Journal of Applied Crystallography

ISSN 0021-8898

Laboratory exploration of mineral precipitates from Europa's subsurface ocean

Stephen P. Thompson,[a]* Hilary Kennedy,[b] Benjamin M. Butler,[c] Sarah J. Day,[a] Emmal Safi[a,d] and Aneurin Evans[d]

[a]Diamond Light Source, Harwell Science and Innovation Campus, Didcot, Oxfordshire OX11 0DE, UK, [b]School of Ocean Sciences, Bangor University, Menai Bridge, Anglesey LL59 5AB, UK, [c]Environmental and Biochemical Sciences, The James Hutton Institute, Craigiebuckler, Aberdeen AB15 8QH, UK, and [d]Astrophysics Group, Lennard-Jones Laboratories, Keele University, Keele, Staffordshire, ST5 5BG, UK. Correspondence e-mail: stephen.thompson@diamond.ac.uk

The precipitation of hydrated phases from a chondritic-like Na-Mg-Ca-SO_4-Cl solution is studied using *in situ* synchrotron X-ray powder diffraction, under rapid (360 K hour^{-1}, T = 250-80 K, t = 3 hours) and ultra-slow (0.3 K day^{-1}, T= 273-245 K, t = 242 days) freezing conditions. The precipitation sequence under slow cooling initially follows the predictions of equilibrium thermodynamics models, however after $\sim$ 50 days at 245 K, the formation of the highly hydrated sulphate phase $Na_2Mg(SO_4)_2{\cdot}16H_2O$, a relatively recent discovery in the $Na_2Mg(SO_4)_2$-H_2O system, was observed. Rapid freezing, on the other hand, produced an assemblage of multiple phases which formed within a very short timescale ($\leq$4 minutes, ΔT = 2 K) and, although remaining present throughout, varied in their relative proportions with decreasing temperature. Mirabilite and meridianiite were the major phases, with pentahydrite, epsomite, hydrohalite, gypsum, blödite, konyaite and loweite also observed. $Na_2Mg(SO_4)_2{\cdot}16H_2O$ was again found to be present and increased in proportion relative to other phases as the temperature decreased. Results are discussed in relation to possible implications for life on Europa and application to other icy ocean worlds.

1. Introduction

Jupiter is the largest planet in the Solar System and has 79 currently identified moons,[1] of which Europa is a lunar-sized body orbiting between the moons Io and Ganymede. Along with Calisto, these are the largest moons, known collectively as the Galilean moons, after Galileo Galilei who, in 1610, was the first to both observe them and to recognise they were satellites to another planet. However, despite these early observations, the existence of a global ocean of liquid water beneath an icy surface is a relatively recent discovery.

Images from the Voyager missions of the 1970s revealed a surface with relatively few craters, indicative of recurrent global resurfacing. Both Voyager and the later 1990s Galileo mission showed Europa's surface to be smooth and criss-crossed by extensive intersecting fractures (Fig. 1) along with other surface structures with diverse morphologies (Pappalardo et al., 1999). While the surface itself is completely frozen, its geology appears consistent with the presence of a subsurface liquid layer, e.g. in places blocks of crust give the appearance of having been pulled apart and rotated within a slushy, or liquid, medium. Measurements of Europa's density suggest a layered interior consisting of a rocky core (possibly with a differentiated inner core of iron), a H_2O-rich layer and ice crust (Nimmo & Manga, 2009; Schubert et al., 2009).

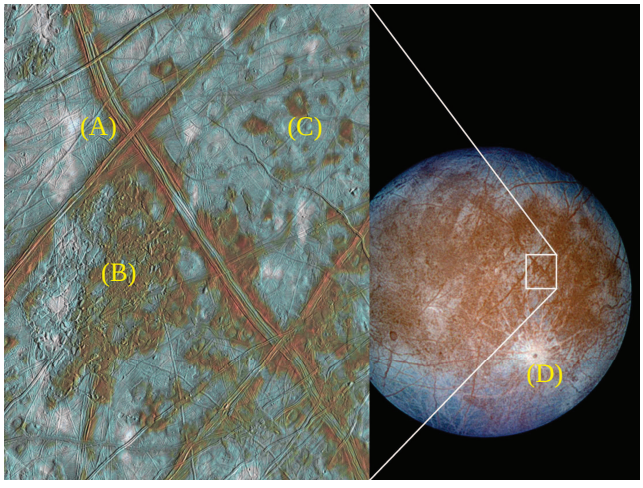

Figure 1
False colour image of Europa's surface taken by the Galileo spacecraft. Reddish-brown areas are non-ice material resulting from surface geologic activity. Icy plains are shown in blue tones. Also visible are (A) long, dark parallel lines comprising ridges and fractures in the crust, (B) chaos terrain, (C) domes and (D) impact craters. Courtesy of NASA/JPL/University of Arizona.

As with the other Galilean moons, Europa likely fomed $\sim$4.5 GYa ago from leftover material following Jupiter's condensa-

[1] https://solarsystem.nasa.gov/moons/jupiter-moons/overview

tion from gas and dust in the early solar nebula, with models (e.g. Travis et al., 2012) suggesting ocean formation occured within the first 0.5 Ga. However, the paucity of large (>10 km) impact craters coupled to a diverse range of surface morphologies points to a dynamic evolution of Europa's ice shell in geologically recent times (∼60 Ma) and are the outward manifestations of both the moon's internal structure and subsurface processes. Spectroscopic observations (Dalton et al., 2005), suggest the presence of an extensive surface mineralogy composed of hydrated salts deriving, at least in part, from the delivery of oceanic water to the surface. As such, the surface mineralogy should provide clues to the subsurface environment and its processes. However, the data thus far does not provide for definitive identifications, due to a combination of several factors – the relatively low resolution of the Galileo instrument, the high noise content of the data itself and the limited number of available library spectra used to make comparisons. Other investigative routes, such as laboratory experimentation, are therefore required in order to provide further physical insights and constraints, as well as identifying potential candidate phases for spectral fitting. Indeed, it was established early on that the rapid freezing and thermal cycling of dilute aqueous solutions of Na_2SO_4, $MgSO_4$ and Na_2CO_3 produced materials that gave near-infrared reflectance spectra that, although distinct from crystalline minerals, bore a resemblance to the spectra of Europa's surface material (McCord et al., 2002).

1.1. The Europan ocean

Evidence of a subsurface ocean was provided by magnetometer readings from the Galileo spacecraft during five close flybys (<2000 km) between 1996 and 2000. Deformations in the geometry of Jupiter's magnetic field were detected that were consistent with the movement, within the field, of a conducting object (Khurana et al., 2009). The perturbations could be fitted to the volume and conductivity of the conducting medium, showing that this could neither be at the moon's centre, nor deep within a rocky core, but rather within ∼30 km of the surface (Zimmer et al., 2000). Furthermore, the electrical conductivity was suggestive of liquid water with a salinity close to that of terrestrial seawater. Surface spectra from Galileo were however noisy, due to the intense radiation generated by Jupiter's magnetic field, but did contain indications of salts consistent with the extrusion of liquid saline water (Dalton et al., 2005). Early proposals for the composition of Europa's ocean centred around three main possibilities, a neutral Na-Mg-SO_4-H_2 solution, an alkaline Na-SO_4-CO_3 solution, or an acidic Na-H-Mg-SO_4 system (Kargel et al., 2000; Marion, 2001, 2002; Kempe & Kazmierczak, 2002).

The pressure at the base of the water layer is within the field of normal ice such that, unlike a number of other icy moons (e.g. Ganymede, see section 4.5.2), the liquid ocean is not sandwiched between low- and high-pressure ice phases, but rather should be in direct contact with the moon's rocky core (Kuskov & Kronrad, 2005). The core itself is expected to be of chondritic silicate composition, having derived from pre-solar materials (Fanale et al., 2001). Although long-lived radioactive elements are likely to be contained within the core, along with residual heat leftover from Europa's collisional formation from smaller bodies, calculations suggest these are insufficient to maintain a liquid ocean of the volume deduced from the Galileo measurements (Schubert et al., 2009). Instead, the main source of heating is the tidal extraction of energy from Europa's eccentric orbit. Although this should, over time, circularise the orbit, the relationship between the orbital periods of Io, Europa and Ganymede (Europa's orbital period is twice Io's and half Ganymede's) allows the eccentricity to be maintained (Sotin et al., 2009) and provides an ongoing supply of energy capable of sustaining a liquid ocean.

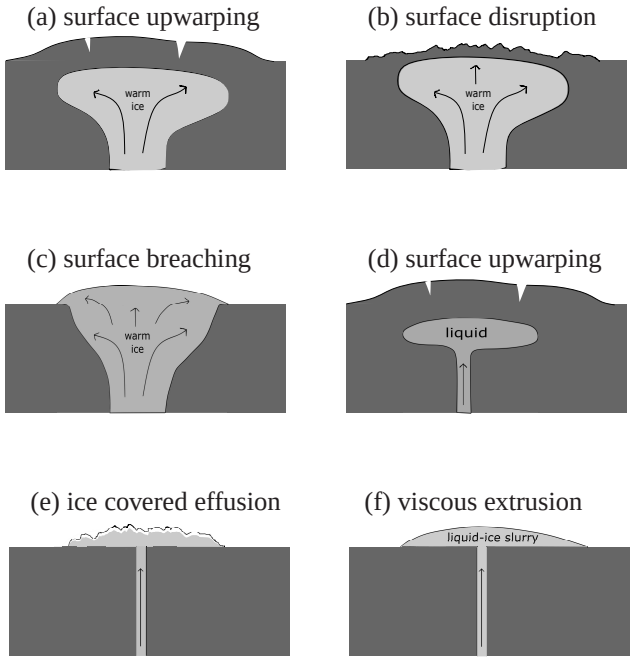

Figure 2
Origin of Europan surface morphologies I: Formation positive surface relief features on Europa involving potential delivery of subsurface ice/water to Europa's surface (Figures after Fagents, 2003). Top panel: diapirism in a thick ice shell leading to (a) surface up-warping, (b) surface disruption, or (c) surface breaching and viscous flow. Surface up-warping and disruption by a rising diapir could also be accompanied by melting and release of near-surface brines (Head & Pappalardo, 1999). Bottom panel: intrusion of injected ocean water in a thin ice shell leading to (d) surface up-warping, (e) ice-covered effusions, or (f) viscous extrusions causing cryolava domes.

The prospect of a global subsurface ocean, that has remained liquid up to the present day, makes Europa a prime target in the search for life beyond Earth (Marion et al., 2003; Greenberg, 2008). As a potential abode for life, Europa meets the three key criteria for habitability: (i) a source of energy, (ii) liquid water and (iii) the availability of biologically essential elements (Priscu & Hand, 2012). Underlying this last criterion is the primary fact that the ocean maintains contact with the rocky core whose chondritic composition means it will be rich in biologically essential elements. As proposed for Earth (e.g.

Martin et al., 2008), hydrothermal vents on the sea floor could provide the original environment in which Europan life could potentially have developed, fuelled by chemosynthesis, or serpentinization (Henin, 2018). These same chondritic materials are of course the source of Europa's ocean salinity (see section 1.3) and, in terms of habitability, the ocean itself is not a particularly extreme environment. Ocean temperatures should lie close to freezing, though the salinity will likely reduce these to around 250 K while, despite being ∼100 km deep, the sea floor pressure should only be ∼110 MPa due to Europa's gravity being less than one-seventh of the Earth's. In this respect, it is equivalent to the pressure in the 11 km deep Mariana Trench on Earth, which, though extreme by Earth standards, is known to support an active and diverse microbial ecology (e.g. Takami et al., 1997; Nunoura et al., 2015, 2018; Tarn et al., 2016). The current observational pressure limit for life on Earth is ∼150 MPa (Hazel et al., 2016), while experiments show viable prokaryotic cells can survive pressurisation (at least over laboratory timescales) into the 2–3 GPa range under static compression. Higher species such as liparid snailfish have also been observed within the Mariana Trench at depths of 8.1 km (Linley et al., 2016), equivalent to a pressure of ∼82 MPa, with their likely maximum depth (∼8.4 km) limited by biochemical factors concerning osmotic regulation in teleost taxa, related to their evolutionary origins in fresh water environments, rather than pressure per se (Yancey et al., 2014; note also that Earth's deep-sea fish lineages likely represent a recolonization from shallower depths following an anoxic extinction event during the Cretaceous period, Priede & Froese, 2013).

1.2. Ocean-surface transport

Five predominant Europan surface terrains have been identified: (i) chaos terrain, (ii) ridges, (iii) plains, (iv) bands and (v) crater terrain (Figueredo & Greeley, 2000, 2004; Greeley et al., 2000). Of these, chaos and ridged plains cover the majority of the surface (Doggett et al., 2009; Greeley et al., 2000; Schenk, 2009) and have led to numerous competing hypotheses to explain their origin and relation to the underlying ocean. For example, for chaos terrain these have included melt-through (Greenberg et al., 1999; O'Brien, 2002), diapirism (Pappalardo et al., 1998a; 1998b; Schenk & Pappalardo, 2004) and the collapse of a melt-lens within the ice shell (Schmidt et al., 2011; Soderlund et al., 2013; Walker & Schmidt, 2015); while for double ridges proposals include cryovolcanism (Fagents & Greeley, 1997; Kadel et al., 1998), tidal squeezing (Greenberg et al., 1998), linear diapirism (Head et al., 1999), shear heating (Nimmo & Gaidos, 2002), compression (Sullivan et al., 1998), wedging (Melosh & Turtle, 2004; Han & Melosh, 2010; Johnston & Montesi, 2014) and compaction (Aydin, 2006); and for ridge-and-trough terrain, extensional tilt-blocks (Kattenhorn, 2002) and folding (Leonard et al., 2015). As well as impact craters, lenticular structures (from the Latin *lenticulae* meaning "freckles") are dotted across Europa's surface and could be suggestive of localised lava domes due to eruptions of viscous icy slurries, successive stacking of thin, fluid flows, inflation of ice-covered water flows, or surface breaching by warm ice diapirs and subsequent flow, or relaxation, of the ice for short distances over the surface.

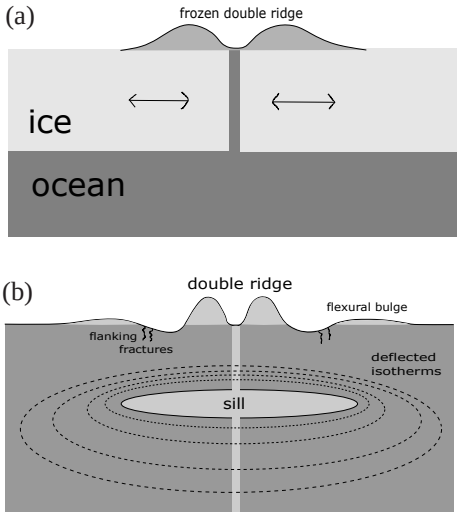

Figure 3
Origin of Europan surface morphologies II: Double ridges. A common feature for which many models have been proposed. These include (a) tidal squeezing, whereby daily tidal forces cause a crack to open and close, pumping material onto the surface (Greenberg et al., 1998); and (b) cryovolcanism, where a pre-existing crack provides a pathway for fissure eruptions that build the ridges cryoclastically (Kadel et al., 1998). In terrestrial volcanic systems the amount of subsurface magmatism tends to exceed the amount of surface volcanism and should also be true on an icy satellite, since the cryomagma (i.e. water) is denser than the surface rock (i.e. ice). Thus while the ridge is being built as a cryoclastic fissure eruption, a cryomagmatic should sill form at a depth corresponding to the neutral buoyancy of water within the ice shell.

These morphological interpretations place demands on the ice shell thickness and is the limiting factor in whether their hypotheses provide for physical ocean-to-surface links to allow oceanic materials to be delivered to the surface. In general, only thin shell models provide for direct ocean-surface contact. Models of Europa's orbit imply its eccentricity and obliquity periodically vary over geological timescales (Hussmann & Spohn, 2004; Bills et al., 2009) and, since tidal heating and the resulting equilibrium shell thickness both depend on these two orbital elements, the thickness of Europa's ice shell is likely to vary over time. There should, therefore, be significant periods when the thickness lies somewhere between two thick/thin extremes. Unfortunately, the shell thickness is poorly constrained by both observations and models. Nevertheless, the expected tidal and radiogenic heat for Europa predict a thickness of 20 to 30 km (Hussman et al., 2002; Spohn & Schubert, 2003), while the physical properties of ice (rheology and grain size) suggest convection within the shell should initiate for thicknesses of 15 to 25 km (McKinnon, 1999). Europa's two largest multi-ringed craters similarly point to a thickness of ∼20 km at their time of formation (Schenk, 2002). More recently, analysis of likely tidal heating, dissipation and conductive cooling suggest an average thickness of 15 to 35 km (Quick & Marsh, 2015; Vilella et al., 2020), while recent analysis of previously unanalysed high resolution images from Galileo suggests local-scale resurfacing

has evolved over time, transitioning from distributed deformation (expressed by the formation of the ridged plains) to discrete deformation (typified by the formation of chaos terrain and isolated fractures) and is likely consistent with progressive shell thickening and cooling (Leonard et al., 2018).

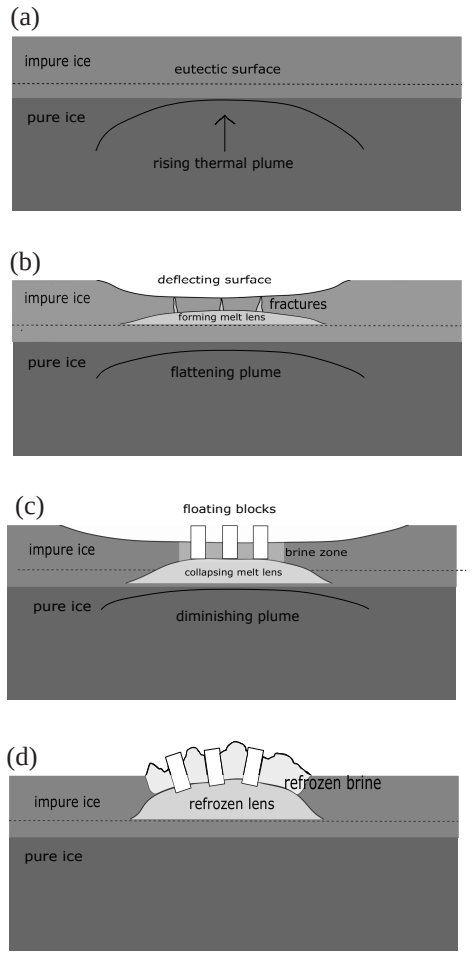

Figure 4
Origin of Europan surface morphologies III: Near-surface melt water during chaos terrain formation: (a) ascending thermal plume in the subsurface approaches the pressure-melting eutectic point of the overlying impure brittle ice; (b) melting causes surface subsidence that hydraulically confines water, and produces tensile cracks; (c) hydro-fracture from the melt lens calves ice blocks, while fracture and brine infiltration forms a granular matrix; (d) Refreezing of the melt lens and freezing of the now brine-rich matrix raises the chaos feature above the surrounding terrain, and can cause domes to form between blocks and at the margins. Figures after Schmidt et al. (2011).

In terms of more localised liquid water existing just below the surface Schmidt et al. (2011) proposed that large-scale chaos features could be explained in terms of near-surface liquid water (but without complete melt through of the ice shell), while Manga & Michaut (2017) proposed a model of microfeature formation that implied present-day near-surface liquid water underneath all pits, some domes and some small chaos features. Similarly, ridge formation proposals include moving liquid water (Dombard et al., 2013; Craft et al., 2016), freezing within the shell (Johnston & Montesi, 2014) and large-scale ice plate motion and subduction (Kattenhorn & Prockter, 2014). For shell thicknesses >20 km whole surface breaching, or melt-through, by sporadic impacts are unlikely (Schenk, 2002), but could cause localised melts or breaches of liquid filled subsurface sills, exposing their contents to freezing surface conditions. Graphical representations of some of the many proposed ocean-to-surface mechanisms are given in Figs. 2 to 5.

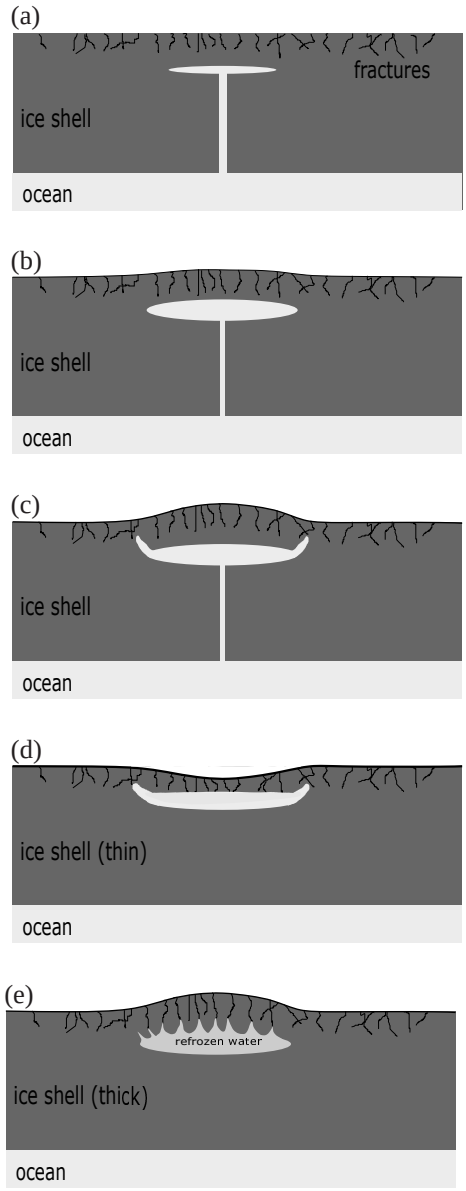

Figure 5
Origin of Europan surface morphologies IV: Evolution of a subsurface saucer-shaped sill and its surface expression, creating pits, domes or small chaos. Upward intrusions into the surrounding ice by freezing water from a sill (a) lead to surface disruption, or extrusion (b and c), to form spots with a subsurface sill (d or e). Figures after Manga & Michaut (2017).

While the forgoing account and illustrations are intended as neither a complete, nor exhaustive, review, for the purposes of this paper it should convey both the wide variety of processes and the range of conditions under which oceanic material could

be transported to the surface, from locations where temperatures of 250-273 K allow water to remain liquid, to highly freezing conditions where temperatures typically range from 110 K at the equator to 50 K at the poles, and encompassing regions and temperatures in between (e.g. within rising thermal plumes or liquid/freezing sills). It should also be clear that there is likely to be a similarly wide range in the timescales in which cooling and freezing occurs, from long-lived, slow-cooling, near-equilibrium processes, likely to occur in long-lived subsurface sills, to rapid, kinetically dominated, flash freezing in eruptive events, typified, for example, by recent observations of active plumes similar to those seen on Enceladus (Roth et al. 2014a,b; Sparks et al., 2016, 2017; Jia et al., 2018).

1.3. Ocean composition

The chemical evolution of a planetary ocean is directed primarily by the object's bulk composition and thermal history (Sohl et al., 2010). The bulk composition comprises the ratios between rock, water ice, non-water volatiles and organic compounds, while the thermal history affects the freezing-thawing cycles, degree of ice melting, extent and duration of chemical interaction between rock and liquid water, degassing of the deep interior and secondary precipitation of organic and inorganic phases. The wide possible variation in these factors leads to a diverse range of possible evolutionary pathways among the ocean-bearing bodies of the Solar System (see reviews by Hussmann et al., 2006; Nimmo & Pappalardo, 2016; Lunine, 2017; and Mann, 2017 for known, probable and plausible ocean-bearing Solar System bodies). Since Europa is subject to ongoing tidal heating, this long-lived heat source means it is likely to experience extensive and prolonged water-rock interactions somewhat akin to hydrothermal systems on Earth, as previously mentioned. Not only do these provide the Europan ocean with its salinity, but are also considered to increase the possibility for life since hydrothermal systems on Earth have long been considered potential genesis locations in origin of life theories (Corliss et al., 1981; Baross & Hoffman, 1985; Holm, 1992).

The potential chemical composition of the Europan ocean can be constrained through possible weathering/leaching reactions and the assumed composition of its carbonaceous chondrite core (McKinnon & Zolensky, 2003). From observational data, Hand & Chyba (2007) suggested a salinity in the range 3-15 g/kg, while to identify the main likely elemental components, Fanale et al. (2001) subjected a sample of the Murchison CM meteorite (carbonaceous chondrite) to hot water leaching to simulate low- to moderate-temperature hydrothermal processing. CM chondrites, although known to have suffered some mineralogical alteration while on their parent bodies, are believed to have retained their original cosmochemical composition (McSween, 1979; Wasson & Kallemeyn, 1988). The leachates were subjected to a series of sequential fractional crystallisation steps, producing a series of ices and brines. Analysis of the brine compositions identified two relationships: (i) for cations Mg$\approx$Na$>$(Ca, K, Fe) and (ii) for anions $SO_4 \gg$Cl. Numerical modelling by Zolotov & Shock (2001), based on a range of chondritic meteorite types, provided general agreement with Fanale et al.'s results. Their suggested model ocean composition had molal concentrations (moles $kg^{-1}_{H_2O}$) of (i) cations: Mg^{2+} 6.271 $\times 10^{-2}$, Na^{+} 4.910 $\times 10^{-2}$, Ca^{2+} 9.637 $\times 10^{-3}$, K^{+} 1.964 $\times 10^{-3}$; (ii) anions: SO_4^{2-} 8.744 $\times 10^{-2}$, Cl^{-} 2.087 $\times 10^{-2}$. This corresponded to molal concentrations of soluble salts $MgSO_4$ 6.271 $\times 10^{-2}$, NaCl 2.087 $\times 10^{-2}$, Na_2SO_4 1.412 $\times 10^{-2}$, $CaSO_4$ 9.637 $\times 10^{-2}$ and K_2SO_4 9.8 $\times 10^{-2}$. The total salinity for this model is 12.3 g/kg and is almost three times less than terrestrial seawater. However, since chondrite meteorites will have suffered varying degrees of parent body processing they may not fully represent the mineralogical make up of Europa's primary material and could potentially produce unrepresentative leachates. It should also be noted that McKinnon & Zolensky (2003) questioned the validity of an $MgSO_4$ dominated ocean, including the assumed initial composition, the relevance of the leaching experiments and the difficulty of forming sulphate in reducing conditions, suggesting instead a ratio by weight of $\sim$10% water ice to $\sim$90% anhydrous rocky material with solar abundances of non-ice elements, which could yield an ocean with a lower sulphate concentration.

Although aqueous differentiation and long-term sea floor leaching of Europa's primary material is generally assumed to produce a system rich in sulphates, more extensive hydrothermal circulation and differentiation of the rocky component on the other hand more likely results in a NaCl-rich ocean (Kargel et al,. 2000), as on Earth. The Saturnian satellite, Enceladus, whose structure (rocky core + subsurface ocean + ice shell) may be similar to Europa's, exhibits active plumes containing NaCl (but not Mg or SO_4, Postberg et al., 2009, 2011) presumably arising from a NaCl-rich ocean (Waite et al., 2006) and H_2 suggestive of hydrothermal activity (Waite et al., 2017). However, since the precise relationship between surface and ocean matter are not established, the presence of NaCl could represent either a body that has undergone more extensive processing than expected, or simply the surface of a compositionally stratified ice shell (Zolotov & Shock, 2001). Furthermore, Na^{+} has also been detected in Europa's tenuous atmosphere (Brown & Hill, 1996) while Mg^{2+} has not (Horst & Brown, 2013). Since the atmosphere results from the sputtering of surface material, this could either constrain the composition, or support a compositional differentiation within the ice shell. However, chloride salts are spectrally inactive over the visible and much of the infrared, including the spectral regions utilized by many spacecraft and telescopes, which both renders them almost impossible to detect, and incapable of accounting for the signatures of hydrated species thus far observed.

The above objections and observations concerning the possible limitations of leaching experiments notwithstanding, the likely chondritic nature of Europa's initial building block materials makes a compelling case and in the present work we assume (section 2.1) an ocean composition closer to that predicted by leaching from a chondritic core.

1.4. Predicted precipitates from cooling Europan brines

The behaviour of a cooling, chondritic-based, Europan ocean was modelled computationally using FREZCHEM by Kargel et

al. (2000) based on a Europan brine whose Mg-Na-Ca-sulphate composition (based on an earlier calculation, Kargel, 1991) was adjusted to include chlorides in the amounts determined by the Fanale et al. (2001) leaching experiments. For an initial solution of given composition, FREZCHEM minimizes the Gibbs free energy of the system and solid phases formed during evaporation or freezing are assumed to have the potential to subsequently dissolve, or react, as the properties of the solution change, with all precipitated phases remaining available for subsequent reactions. This represents equilibrium crystallisation and the recrystallising phases can gain or lose waters of hydration, altering both the ionic composition and concentration of the solution. Kargel et al. (2000) also investigated the possibility of fractional crystallisation whereby precipitated phases are buried by other precipitating salts and therefore unavailable for any further reactions. In equilibrium freezing, magnesium sulphate first precipitates as $MgSO_4{\cdot}7H_2O$, but is completely replaced by $MgSO_4{\cdot}11H_2O$ via reaction with the brine as it cools, while in fractional crystallization $MgSO_4{\cdot}7H_2O$ is preserved and then buried by $MgSO_4{\cdot}11H_2O$ and other salts.[2] The loss of sulphate enriches the remaining brine in chloride. The uptake of hydration waters and the precipitation of ice also contribute to this enrichment. The enrichment in Cl is particularly noticeable because, unlike all other ions, until hydrohalite precipitates at the eutectic, there is no removal of Cl from the brine.

Fractional and equilibrium crystallization produced very similar brine-precipitate sequences that varied only in the fine details of temperature and relative composition (plus an additional $MgCl_2{\cdot}12H_2O$ phase for fractional crystallisation). The general order of precipitation with decreasing temperature for the European brine system predicted by Kargel et al. is:

$$\begin{gathered}
T = 298\ \text{K} \\
MgSO_4{\cdot}7H_2O\ \text{(epsomite)},\ CaSO_4{\cdot}2H_2O\ \text{(gypsum)} \\
\downarrow \\
T = 286\ \text{K} \\
Na_2SO_4{\cdot}10H_2O\ \text{(mirabilite)} \\
\downarrow \\
T = 271\ \text{K} \\
MgSO_4{\cdot}11H_2O\ \text{(meridianiite)} \\
\downarrow \\
T = 266\ \text{K} \\
\text{ice} \\
\downarrow \\
T = 238.65\ \text{K} \\
NaCl{\cdot}2H_2O\ \text{(hydrohalite)}.
\end{gathered}$$

After hydrohalite the eutectic temperature is reached, below which liquid water cannot exist. The main feature of this sequence is that at higher temperatures the precipitates are dominated by sulphate phases. Both equilibrium and fractional crystallisation showed an enrichment of chlorides at lower temperatures, with a crossover between chloride and sulphate abundances at about 266 K, close to the temperature where ice begins to precipitate, and following the point where the amount of water held in precipitated salts crosses over to exceed that held in liquid water (∼268 K). The colder the ultimate temperature, the higher the final Cl/SO_4 ratio. These results were replicated by Marion et al. (2003, e.g. Fig. 5), while Zolotov & Shock (2001), using a more dilute starting solution, found $MgCl_2{\cdot}12H_2O$ was the last salt to precipitate, rather than $NaCl{\cdot}2H_2O$.

Table 1
Chemical formula, mineral name, abbreviation and density information (from ICDD PDF-4$^+$ database) of phases identified in the MEOS precipitate.

phase formula	mineral name	abbreviation	density (g/cm^3)
H_2O	water ice	Ih	0.931
Mg phases:			
$MgSO_4{\cdot}5H_2O$	pentahydrite	MS5	1.929
$MgSO_4{\cdot}7H_2O$	epsomite	MS7	1.679
$MgSO_4{\cdot}11H_2O$	meridianiite	MS11	1.512
Na phases:			
$NaCl{\cdot}2H_2O$	hydrohalite	NC2	1.654
$Na_2SO_4{\cdot}10H_2O$	mirabilite	NS10	1.465
Ca phases:			
$CaSO_4{\cdot}2H_2O$	gypsum	CS2	2.307
Na-Mg phases:			
$Na_2Mg(SO_4)_2{\cdot}4H_2O$	blödite	NMS4	2.223
$Na_2Mg(SO_4)_2{\cdot}5H_2O$	konyaite	NMS5	2.098
$Na_{12}Mg_7(SO_4)_{13}{\cdot}15H_2O$	loweite	NMS15	2.364
$Na_2Mg(SO_4)_2{\cdot}16H_2O$	–	NMS16	1.623

2. Experimental details

Given the wide range of possible hydrated mineral phases within the Na-Mg-Cl-SO_4-H_2O system, the numerous complex pathways that exist between them and the varied means by which oceanic waters may be delivered to the surface, equilibrium thermodynamics may not be sufficient to model the behaviour of a large percentage of Europa's oceanic waters once delivered to surface and near surface regions. Consequently, in this paper the two experimental regimes of slow freezing and rapid freezing of a model Europan ocean solution (MEOS) are employed to probe the effects of equilibrium and non-equilibrium freezing conditions on precipitation behaviour.

2.1. MEOS composition

As discussed in section 1.3, Europa's ocean likely lies within the Na-Mg-Ca-Cl-SO_4-H_2O system, though the precise relative concentrations are only weakly constrained. For the present work we have used a MEOS based on the general carbonaceous chondrite meteorite composition suggested by Kargel (1991) with a chloride content suggested by Fanale et al. (1998). 1 kg of MEOS was prepared gravimetrically (to 2 decimal places, g) using distilled water, recrystallised analytical grade salts (Mg_2SO_4, Na_2SO_4 and NaCl) and an aqueous solution (∼1 mol kg_{sol}^{-1}) of $CaCl_2$ (characterised by potentiometric titration, Papadimitriou et al., 2013). The $CaCl_2$ was prepared as a solution due to its hygroscopic nature in laboratory conditions. The

[2] Prior to 2006, when the correct hydration state was recognised, $MgSO_4{\cdot}11H_2O$ is referred to in the literature as $MgSO_4{\cdot}12H_2O$

MEOS was prepared to a molal composition (mol $kg^{-1}_{H_2O}$) of Na = 1.630, Mg = 2.929, Ca = 0.0064, Cl = 0.308 and SO_4 = 3.5964 (Marion et al., 2005).

2.2. Data collection, reduction and analysis methodology

In situ synchrotron X-ray powder diffraction measurements were performed on beamline I11 (Thompson et al., 2009) at the Diamond Light Source. This is an undulator beamline with two experimental hutches in tandem. The first (EH1) houses a large 3-circle diffractometer equipped with a fast position sensitive detector (PSD) designed for *in situ* and in operando experiments, particularly under non-ambient conditions (Thompson et al., 2011). The PSD consists of 18 Mythen-II Si-strip detector modules tiled around a 90° arc. For the present work, to compensate for the small gaps between modules, while providing time and temperature resolution, each 10 s dataset comprised two 5 s exposures, offset by 0.25° 2θ and automatically merged together by the data acquisition system. The X-ray energy was 15 keV (0.824603 Å, calibrated against NIST 640c Si reference powder). The second hutch (EH2) houses the *Long Duration Experiments* (LDE) facility (Murray et al., 2017) and is dedicated to the study of slowly evolving systems, again particularly under non-ambient conditions. Its operating energy is 25 keV (0.49388 Å, calibrated average for the experimental run), to provide cell/sample penetration, and detection is by area detector (Pixium), with 2D patterns obtained by integration around the image centre point. The LDE facility was used to house a cold cell designed for studies of hydrated mineral precipitation from slowly cooled aqueous solutions (Thompson et al., 2018, see also section 2.2.2 below).

2.2.1. Fast in situ cooling experiment. Portions of MEOS were injected into a 0.5 mm diameter borosilicate capillary tube. This was placed within a brass holder and sealed at the holder end with wax. The other end was left open, with fluid being retained by capillary action, in order to avoid the build-up of excess pressure during isochoric freezing (e.g. Yakovlev & Downing, 2011). The holder then sits on the spinner stage located at the centre of the EH1 diffractometer. An Oxford Cryosystems liquid nitrogen cryostream was mounted on a separate motorised table and aligned such that its nozzle envelops the length of the capillary up to the point adjacent to where the X-ray beam impinges (Fig. 6(top)). The sample temperature was ramped from 256 K down to 80 K in 2 K steps (with 6 K min^{-1} ramp rate between steps, $\pm$0.1 K at each step) and was allowed to equilibrate for 1 minute at each step prior to data collection. The time-temperature profile for the experiment is shown in Fig. 7a.

Topas[3] was used to perform whole pattern Pawley fits to the diffraction data according to the following reductive procedure:

(i) candidate phases with compositions based on the chemical composition of the solution were individually refined against the measured data,
(ii) those that (a) provided fits to some of the Bragg peaks, (b) did not result in an unrealistically deviated background function in order to compensate for their intensity contribution and (c) did not introduce peaks in the fit that were absent in the data were accepted,
(iii) the phase with the lowest R_{wp} was the taken as the starting fit and the remaining phases individually added in and refined against this,
(iv) of these, the phase that then gave the best reduction in R_{wp} was retained and added into the fit.

This process was then repeated until adding any of the remaining phases failed to improve the fit (i.e. increased R_{wp}). The candidate phases and their starting lattice parameters were taken from published sources and the ICDD PDF4$^+$ database. The maximum 2θ was limited to $\sim$20° in order to prevent higher angle data, where Bragg peaks from the various salt phases become severely overlapped, adversely influencing the fit.

2.2.2. Slow in situ cooling experiment. The LDE cold cell is shown in Fig. 6(middle). The sample chamber (Fig. 6(bottom)) is constructed from two bolt-together solid copper body components with two 6 mm diameter circular apertures for beam transmission. The MEOS is contained by two 0.05 mm thick diamond windows and two 0.5 mm thick, 7 mm inner diameter silicone O-rings, such that the sample fluids do not come into direct contact with the copper body (Fig. 6(bottom) inset). The sample blocks are encased by nine horizontally stacked Palight PVC foam boards, 25 mm thick, each having a divergent 0.025 mm Kapton window to provide an insulating multi-glazing effect while allowing diffracted X-rays to pass. A Lauda ECO RE1050 chiller unit (GOLD control head) is used to flow 60:40 glycol antifreeze and demineralized water refrigerant through the blocks in closed circuit. The cell temperature is thus regulated via the chiller which is itself controlled externally, in open loop, using a computer script running on a dedicated EPICS input/output controller. Given a starting temperature, ramp rate and the total number of days over which the cell is to be cooled, the script calculates and updates the required chiller setpoint temperature every 5 s to give a programmed cooling ramp. A rate of 0.3 K day^{-1} allows a reasonable difference in temperature to be achieved within the weekly measurement regime of the LDE facility (see Murray et al., 2017). Fig. 7(bottom) shows the time-temperature profile for the slow cooling experiment.

Prior to the start of the experiment, the detector-sample distance was set to 350 mm, sufficient to give a reasonably wide 2θ range of 42° for energy calibration. The centre position of each cell was determined by scanning the cell chamber both horizontally and vertically through the beam and recorded in a data acquisition script. The chamber then returns to the same position each week and diffraction data collected at this optimal in-beam position and at four additional vertical positions offset by $\pm$1-2 mm. The beam size was 200 μm $\times$200 μm achieved by slitting down the incident beam. Each week, using a built-in CeO_2 reference standard, the wavelength and detector distances were automatically refined using the data reduction pipeline that incorporates the DAWN software suite (Filik et al., 2017) which was also used to automatically integrate and convert the 2-D

[3] http://www.bruker-axs.com

images into conventional 2θ versus intensity ASCII files.

Large crystals forming in the sample chamber can result in very intense diffraction spots occupying a significant area of the detector. While it is, in principle, possible to mask these out prior to integration, the volume of data accumulated and the variability in their occurrence from week to week (such that a new mask would need to be drawn for each image) meant that this was not a feasible option in the first instance; while simple thresholding produced variable results such as halo artefacts, missed spots and loss of legitimate signals. Instead, as discussed in Thompson et al. (2018), the images were first integrated into separate 1-D data files and visually inspected. Those showing broad and intense, non-background, features were rejected (typically 1-2 images per week), while the remaining data were averaged to produce a single data file for each week.

Data analysis for the slow-cooling experiment followed similar lines to the fast *in situ* experiment, but with several pre-processing steps. The wavelength, obtained from the CeO_2 reference sample, was used in conjunction with the Bragg peaks from the cell's diamond window to refine and fix the zero point for each weekly dataset. Next, due to the medium-low resolution nature of the data, only the low angle peaks up to the first diamond peak at $\sim 14^\circ$ 2θ were considered in the phase fitting process. This is because similarities in the symmetries and unit cell dimensions of various salt phases yield highly overlapped peaks at higher angles which do not allow for unique fits, but can exert unwarranted statistical influence over the fit. At lower angles the Bragg peaks are sufficiently separated in that qualitative phase identifications can be made, even if more quantitative fractional contributions to the scattering cannot be obtained from the fits.

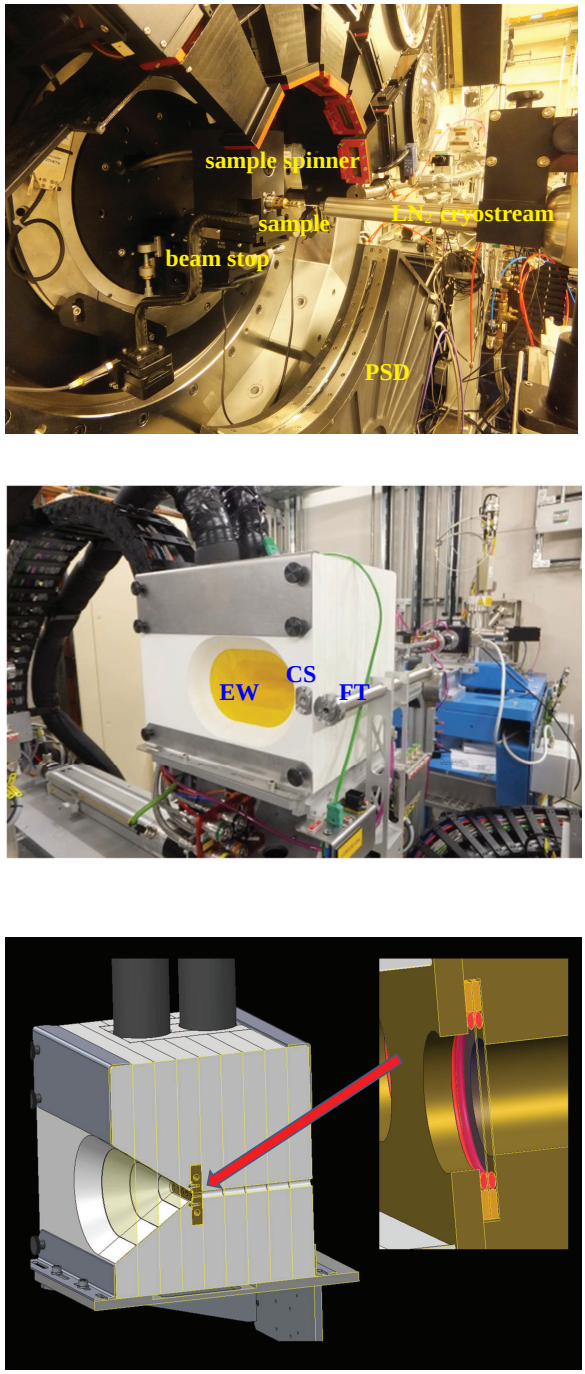

Figure 6
Experimental apparatus. Top panel: *in situ* fast-freeze measurements, view is towards the incident X-ray beam showing sample capillary, orientation of the liquid nitrogen (LN_2) cryostream and position sensitive detector (PSD). Middle panel: Slow *in situ* cooling-rate cold cell installed in the I11 Long Duration Experiments facility, view is towards the incident beam direction and shows the large exit window (EW), calibration standard (CS) housing and X-ray flight tube (FT) for when other long duration cells are being measured. Bottom panel: schematic showing the cold cell's interior sample chamber formed by diamond windows held between o-rings and mounted in a cooled copper block, located within the large insulated housing. (full details given in Thompson et al., 2018).

3. Results

For ease of presentation, we adopt the following abbreviations: sulphate and chloride phases will be denoted by XS*n* and XC*n* respectively, where X represents cations (M=Mg, N=Na and C=Ca) and *n* signifies the waters of hydration. For example, $MgSO_4 \cdot 7H_2O$ and $NaCl \cdot 2H_2O$ will be denoted by MS7 and NC2 etc. (Table 1).

3.1. Fast-freeze experiment

Fig. 8(Top panel) shows three successive diffraction patterns separated in temperature by 2 K and in time by 4 minutes. Contrary to the predictions of equilibrium cooling (section 1.4) the first crystalline phase observed here is due to hexagonal ice. However, as the figure shows, these initial peaks are quickly followed by a complex collection of diffraction features from other solid phases. The bottom panel of Fig. 8 shows a waterfall style plot of the diffracted intensity throughout the whole experiment and shows that, once formed, all phases not only remain present throughout the experiment, but that no further phases are subsequently precipitated.

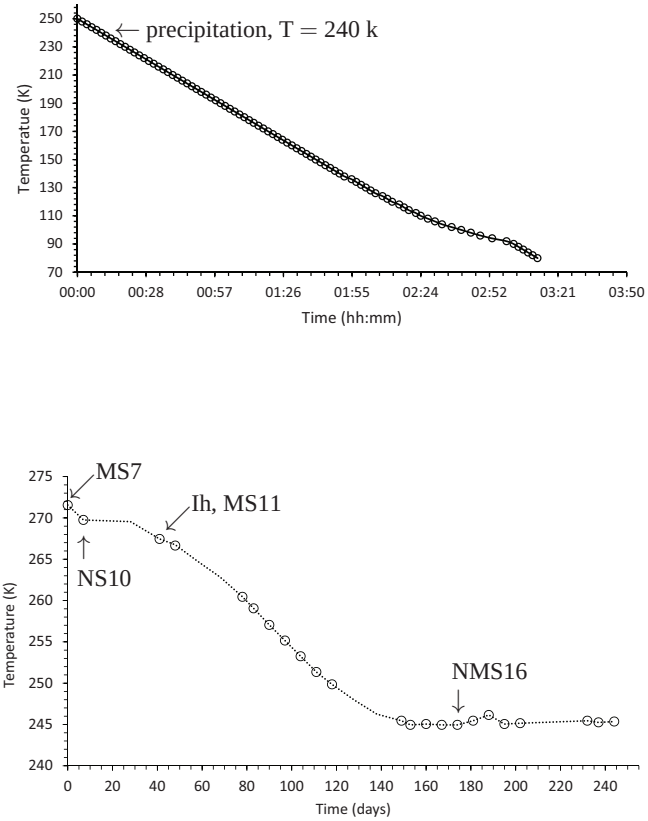

Figure 7
In situ time-temperature profiles for fast (Top Panel) and slow (Bottom Panel) cooling experiments. In both plots the open circles represent the points at which diffraction data were collected. In the bottom panel the dotted line represents the temperature profile of the cell based on the temperature recorded at the start of each day. The short plateaux after the second diffraction point is due to a networking failure early in the experiment such that the cell remained at constant temperature. The gaps between diffraction data points at 20, 60, 130 and 220 days are due to scheduled synchrotron shutdowns. The small rise in temperature at ∼190 days is due to ice build-up in the chiller resevoir which restricted coolant circulation until being removed.

Using the fitting procedure outlined in section 2.2.1, the scattering phases were identified (e.g. Fig. 9(top)) and are listed in Table 1, while the temperature dependency of the scattered intensity for each phase is shown in Figs. 10 and 11 along with Fig. 12 for the corresponding percentage proportion each phase contributes to the total (crystalline) scattered intensity. The intensity of a given phase depends on both the structure factor and the amount of the phase present, so while the relative proportions provide a simple approximation to the major/minor contributors to the scattering, in the absence of Rietveld fitting, relative qualitative changes in the individual phase abundances are better represented by changes in the intensities. The intensity plots have been grouped according to:

(a) the two main contributors MS11 and NS10;
(b) NMS16 and NMS15, which show increasing intensity with decreasing temperature;
(c) MS7, NMS4 and CS2 which show no major change in intensity, along with MS5 which appears approximately constant below ∼130 K;
(d) NC2 and NMS5 which, along with ice, decrease in intensity with decreasing temperature.

By the end of the experiment the two main phases contributing to the diffracted signal are MS11 and NS10, which account for ∼45% of the scattered intensity. Two significant temperatures appear in the figures, firstly at about 200-220 K where many of the precipitated phases show either a maximum, or minimum, in their intensities, and secondly, between 140-160 K where for several phases (e.g. MS11, NS10, NMS16, NMS5) their intensities tend to either level off, or decrease/increase more smoothly. Above ∼160 K, the relative collective behaviour of the precipitated phases appears complex, possibly suggestive of phase instabilities with significant solid-solid and solid-liquid interactions. In general though, the overall trend throughout the experiment is for the minor phases with high hydration states (NMS15, NMS16) to increase in pro-

portion, while those of low, or intermediate, hydration (NMS5, NC2, CS2, MS7 and MS5) either decrease, or remain essentially constant.

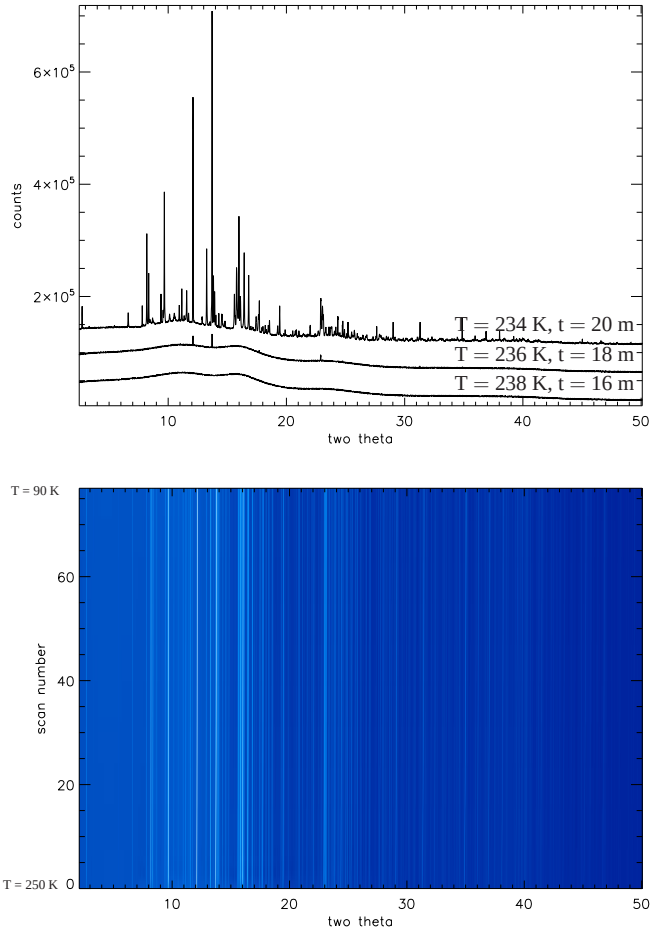

Figure 8
Top panel: successive SXPD patterns showing crystallisation of MEOS under fast-cooling conditions. Data collected at 15 keV (0.824603Å), patterns are offset for clarity, bottom trace is the liquid phase at a temperature of 238 K, reached 16 minutes after the start of the cooling ramp; middle trace show formation of hexagonal ice phase 2 minutes later at 236 K, followed after another 2 minutes by the top trace which shows crystallisation of multiple hydrated phases at 234 K. Bottom panel: waterfall-type plot of diffraction patterns, showing consistency of the phase assemblage once formed. Note, due to colour map stretching to show both weak and strong features, relative variations in intensity for individual peaks are not visible.

The two major phases MS11 and NS10 however show a slightly different pattern of behaviour. NS10 initially shows a significant decrease until ∼200 K, below which its intensity recovers to a level higher than that of its initial formation, appearing to approach a steady state below 160 K. MS11 on the other hand is not a major component of the very first precipitate, but very quickly grows in intensity in the subsequent temperature step. However, as the temperature subsequently decreases it shows a slight oscillatory decline-and-recover behaviour, suggesting at higher temperatures it may be unstable relative to other phases, until ∼180 K, where its intensity appears to level off. As the temperature drops below ∼160 K MS11 shows a smooth recovery to just above its original high level.

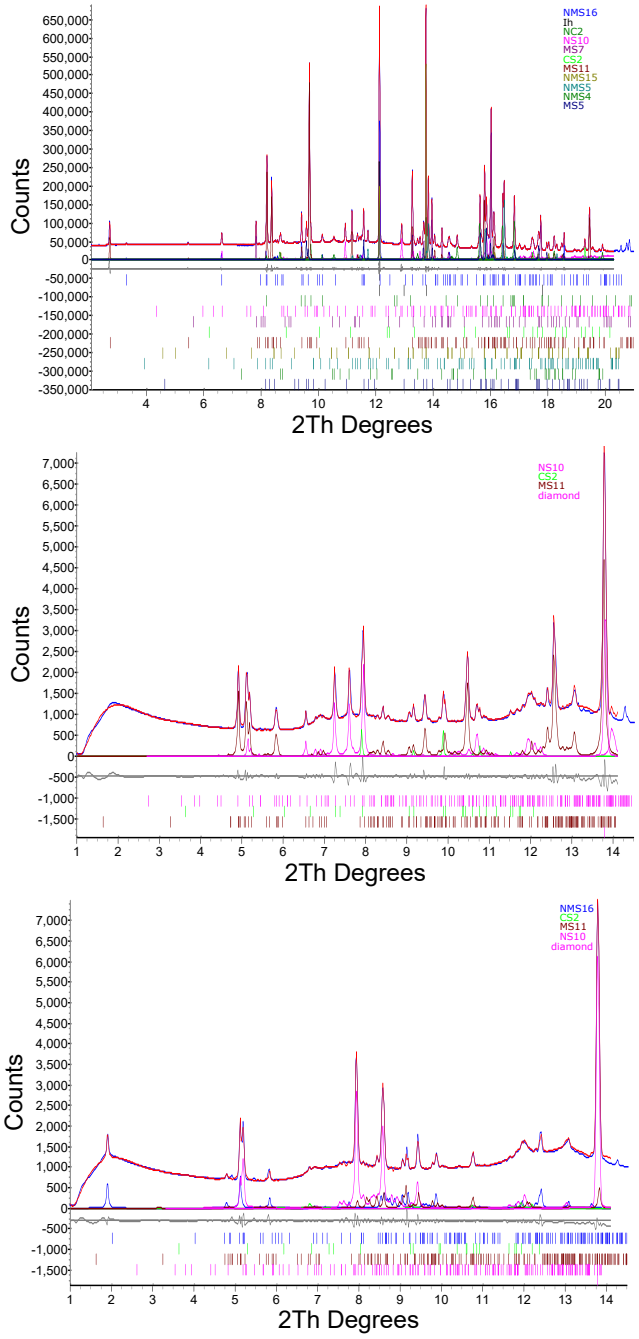

Figure 9
Examples of fits (red line) to XRD data (blue), along with individual phase contributions, obtained for fast (top panel) and slow (middle and bottom panels) cooling rate experiments. The two slow cooling rate patterns were collected two weeks apart on days 167 and 181, respectively, of the long-duration experiment and show the development of NMS16 via the Bragg peak at ∼2° 2θ, as also indicated in Fig. 7. Data collected at 15 keV (0.824603 Å) and 25 keV (0.49388Å, average) for the fast and slow cooling rate experiments respectively

The observation of NMS16 as a precipitate in this system is noteworthy as it is a hydrated phase that has only relatively

recently been reported (observed to form from NMS4 at low temperature, Leftwich et al., 2013, see discussion in section 4.1 below) and as such would not have been predicted by the FREZCHEM models, discussed in section 1.4, that predated its discovery. The presence of this phase is evidenced by the appearance of a Bragg peak at $\sim 3.3^\circ$ 2θ (d-space $= 14.252$ Å) in Fig. 9(top) and more clearly in Fig. 14. As a highly hydrated phase, NMS16 is also one of the phases whose intensity, and therefore quantity, appears to increase with decreasing temperature.

Zolotov & Shock (2001) predicted the formation of $MgCl_2{\cdot}12H_2O$ at the Eutectic temperature of 237.05 K. However, as discussed above, following the initial freeze we do not observe the formation of any new phases and, even though the rapid cooling experiment passed through the eutectic point 14 minutes after the initial 250 K starting temperature (where the sample was still liquid, see section 4.1) and a base temperature of 80 K was reached 3 hours 13 minutes later, we did not observe the formation of any $MgCl_2 \cdot nH_2O$ ($n = 2, 4, 6, 8, 12$) phases. We do however observe the presence of NC2, which is consistent with the prediction (section 1.4) of Marion et al. (2003).

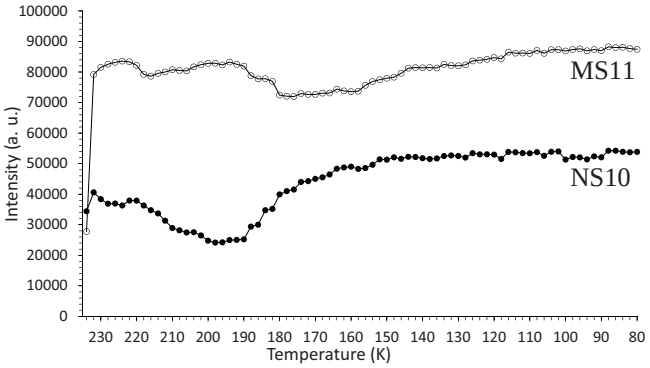

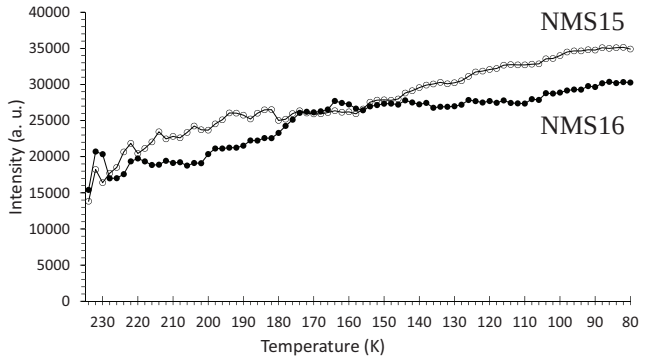

Figure 10
Rapid cooling I: total scattered intensity per precipitated phase at each temperature step for Top panel: main phases MS11 and NS10 and Bottom panel: NMS15 and NMS16.

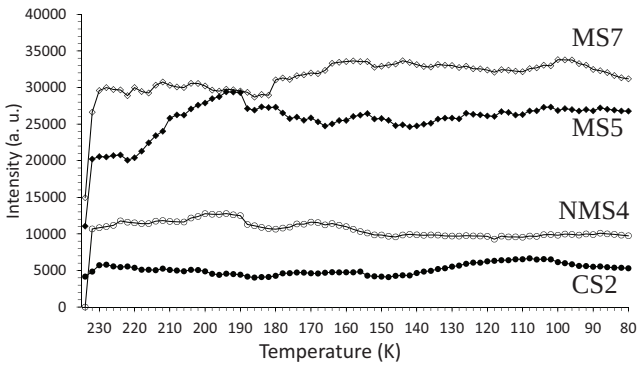

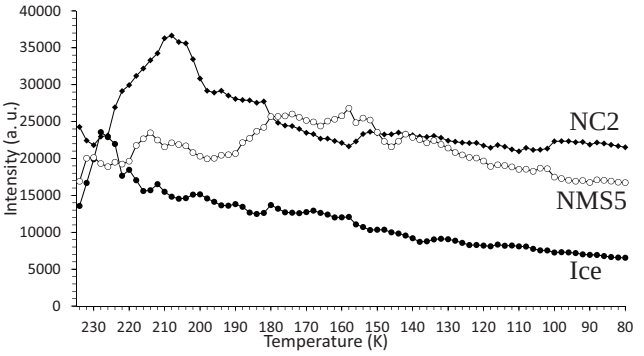

Figure 11
Rapid cooling II: total scattered intensity per precipitated phase at each temperature step for Top panel: MS7, MS5, NMS4, CS2, and Botton panel: NC2, NMS5 and ice.

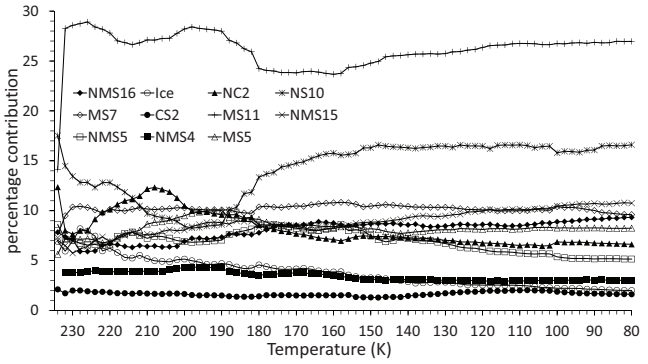

Figure 12
Rapid cooling: the proportional percentage contribution of each phase to the scattered intensity as a function of temperature.

3.2. Slow-freeze experiment

Using the reduction and analysis procedure outlined in section 2.2.2 (see also Fig. 9(middle and bottom) for example fits), the following precipitation sequence was observed for the slow-freeze cold cell experiment:

$$\underset{\text{MS7}}{\overset{T=273K}{\longrightarrow}} \underset{\text{NS10}}{\overset{T=269K}{\longrightarrow}} \underset{\text{Ih \& MS11}}{\overset{T=252K}{\longrightarrow}} \underset{\text{NMS16}}{\overset{T=245K}{\longrightarrow}} \quad (1)$$

These are also indicated on the experiment's time-temperature profile in Fig. 7. The order of precipitation up to MS11 follows that of equilibrium cooling (section 1.4). This also predicts that ice is not the first solid phase to form which, unlike the rapid-freeze experiment, is what we observe. On the other hand we did not detect CS2 precipitation, but this could also be due to a combination of low Ca^{2+} concentration, formation of an amorphous precursor phase (see below) and/or small beam sampling (see discussion in section 4.1). At $\sim$245 K the base temperature of the cold cell is above the predicted eutectic point for this system and consequently we do not observe NC2. However, after a long period of time at base temperature we do observe the formation of the highly hydrated NMS16 phase, again evidenced most clearly the formation of a low-angle Bragg peak at $\sim 2^\circ$ 2θ (d-space $= 14.19$ Å) in Fig. 9(bottom), which was absent from data collected earlier in the experiment (Fig. 9(middle)).

It was not possible to extract detailed information on the relative time-varying abundance of each phase, as per the rapid freeze experiment, due to a combination of systematic and physical factors. Firstly, the formation of large crystals results in multiple large diffraction spots in the area detector images with diameters far wider than the powder rings, that varied in both size and position from week to week. As discussed, these images were rejected from the data reduction process. Secondly, the beam size, necessary to obtain reasonable peak resolution in the LDE geometry was very small (200×200 μm) relative to the total sample volume (10 mm diameter $\times$ 1 mm thick), such that crystallites forming within the sample fluid could potentially sink out of view, resulting in sedimentation, particularly as ice is not the first phase to form. We assume that once ice formation takes place it occurs throughout the whole sample volume, such that any remaining high-salinity fluids are contained within inclusions within the ice, precipitation within these could potentially lead to similar sedimentation effects. Although we have not measured the size of inclusions within our sample chamber, crystallite movement may be a reasonable assumption. Early studies on sea ice found brine pockets as small as $\sim$few$\times$0.1 mm in size (Perovich & Gow, 1996), while more recent magnetic resonance imaging of sea ice cores found brine inclusion diameters as large as $\sim$2 - 6.5 mm (Galley et al., 2015). We assume therefore brine pockets larger than the beam size could also exist within the cold cell following ice formation. Although these effects were mitigated by collecting data at multiple positions within each sample area, the automated nature of the LDE data collection process meant that these were (a) fixed positions and (b) limited in number (four locations per each of the cold cell's five sample chambers, each running a separate experiment) due to the constraints imposed by the time slot allocated to individual experiments running on the multi-experiment LDE facility (Murray et al., 2017). The rejection of whole images ultimately results in a reduction in the gathered information, such that in some weeks a given phase, though present within the cell, could be under, or over, represented in the remaining data, or indeed in some instances not represented at all. Similarly, weak intermediate or metastable phases could also be missed, however, since the precipitation order primarily follows the predicted equilibrium sequence, the likelihood of such phases forming may be small.

It is also conceivable that at these relatively high temperatures the cooling precipitate-brine system is relatively dynamic and that over the course of a week (the time between measurements, with ΔT=2 K) a significant amount of reaction and/or exchange could occur between precipitated phases, and between the precipitates and the remaining brine (e.g. dissolution, loss or gain of H_2O). In studies relating to surface salts on Mars, dehydration experiments at near- and sub-ambient temperature conditions ($\sim$263-252 K) identified the formation of amorphous hydrated Mg-sulphate (e.g. Vaniman et al., 2004; Wang et al., 2006; Dalton, 2012) and related phases (e.g. Sklute et al., 2018). In the case of aqueous systems the nucleation of crystallites is a complex process that involves ion dehydration, close approach of like charges and the arrangement of ions and molecules into ordered 3-D structures (Kashchiev & van Rosmalen, 2003). The precipitation of amorphous phases on the other hand requires less stringent constraints (Vekilov, 2010) and therefore have long been considered a plausible precipitation route for many crystals, as has been extensively demonstrated for calcium carbonate and calcium phosphate (e.g. Addadi et al., 2003; Günther et al., 2006; Combes & Rey, 2010; Bots et al., 2012). It is not inconceivable therefore that phases in the MEOS system could also precipitate via initially amorphous structures. Indeed CS2 has been shown to precipitate via an amorphous CS phase, transforming to CS0.5 and subsequently CS2 (Wang et al., 2012; Stawski et al., 2020). Any putative amorphous phase that formed either by precipitation or partial dissolution would be difficult to distinguish using X-rays, but could react with both the remaining liquid brine and crystalline precipitates.

Qualitatively, MS7's contribution to the scattered intensity did appear in general to be reduced once MS11 had formed, consistent with the prediction that MS7 is replaced by MS11 (Kargel et al., 2000). In our previous study of an $MgSO_4$-H_2O system using this sample cell (Thompson et al., 2018), we similarly observed a slowly changing MS7/MS11 ratio and found that fits could be improved by the inclusion of an amorphous sulphate component to better model the background scatter. In addition, the strength of the background signal showed a steep rise below 250 K, which from the pattern of the diffuse scatter in the original area detector images was attributed to amorphous ice. This likely formed by residual water, with reduced salinity resulting from the precipitation of the salt, undergoing rapid freezing (see Fig. 8 in Thompson et al., 2018 and discussion in sections 4.3 and 5.1 of that paper). In Fig. 13(top) the background signal for the slow-cooling MEOS experiment is

shown and records a similar steep rise in the region of 250 K, suggesting a similar effect is in operation in this system.

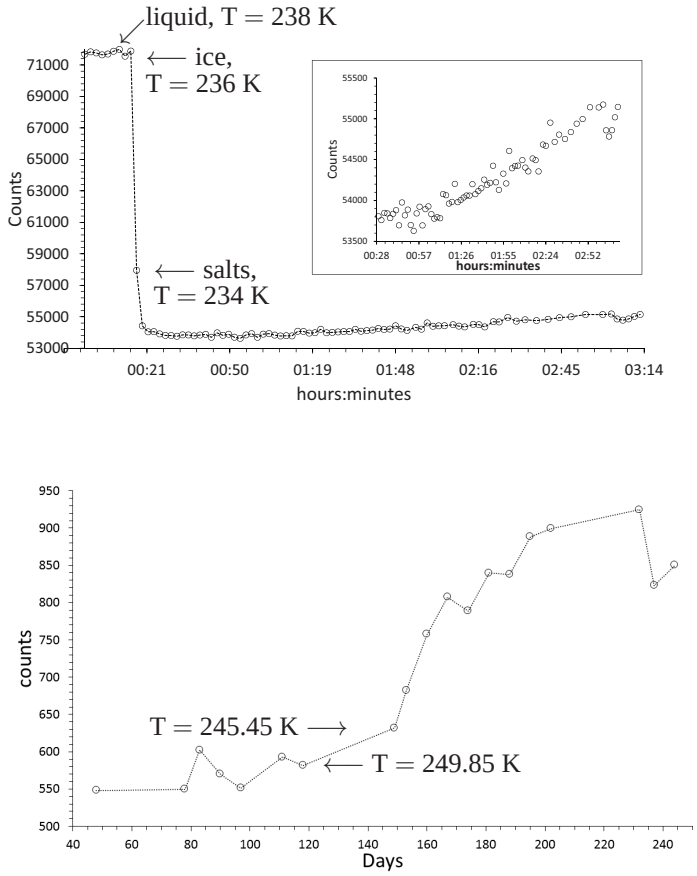

Figure 13
Changes in diffuse scattering background for the rapid cooling experiment, showing (Top panel) change from liquid to ice to the precipitation point of salt phases. After an hour, at ∼175 K there is an increase (inset) in diffuse scatter due to an increase in static disorder at low temperature related to increased rigidity of the bonded water molecules in the salt phases; (Bottom panel) slowly-cooled experiment, the rise in diffuse scatter occurs between 120 and 150 days at or near base temperature for the cell (245 K), suggestive of an increase due to an amorphous phase resulting from the freezing of liquid water at low temperatures likely resulting from a reduction in salinity due to precipitation of salt phases. See discussion in section 3.2.

The background signal for the rapidly cooled MEOS however shows a very different behaviour (Fig. 13(top)). Initially, in the liquid state, a high signal level is recorded, but drops significantly over the course of three data collections as ice forms and salts subsequently precipitate, all within the space of a 4 K drop in temperature. Below ∼195 K (Fig. 13(top, inset)), the background shows a smooth, but weak, rise as the temperature decreases further. Although it is conceivable that the slow rise could be due to the release (and freeze) of water molecules as the various hydrated phases grow, shrink and transform etc., we suggest the smooth variation is more characteristic of a solid-state structural effect caused by the freezing-in of static disorder, due to increases in molecular rigidity involving the waters of hydration, as the temperature drops. Studies of the ∼3500 cm^{-1} hydration band, in the Raman spectra of various sulphates at room temperature, report a band that is broad and smooth (e.g. Wang et al. 2006). This is due to the stretching of O-H bonds, located within a range of crystallographically distinct sites, such that the shape of each structural water is severely distorted from that of a free water molecule. High numbers of structurally incorporated waters, coupled to a wide variation of O-H bond lengths, results in the smearing out of individual band components (Wang et al., 2006). At lower temperatures however, fine structure is observed to form within the band suggesting a restriction in the ranges over which individual water molecules are distorted, likely due to the relative strengthening of the hydrogen bonds as the temperature is decreased, essentially causing the water molecules to become more rigid. Under fast cooling, the rapid imposition of rigidity upon the water molecules should therefore introduce static disorder, giving rise to an increase in diffuse scatter.

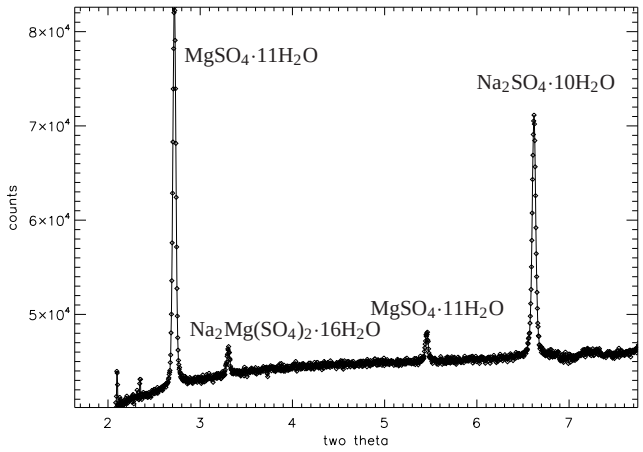

Figure 14
The 001 peaks of the highly hydrated salt phases NMS16 ($Na_2Mg(SO_4)_2{\cdot}16H_2O$), MS11 ($MgSO_4{\cdot}11H_2O$, meridianiite) and NS10 ($Na_2SO_4{\cdot}10H_2O$, mirabilite). The peak at 5.446° 2θ is the MS11 002 peak. The two peaks at 2.098° and 2.349° 2θ are unidentified. Data collected at 15 keV (0.824603 Å).

4. Discussion

4.1. Formation of $Na_2Mg(SO_4)_2{\cdot}16H_2O$ as a Europan mineral

NMS16 was first reported by Leftwich et al. (2013) as a low temperature phase derived from deliquesced NMS4 held below 10 °C for up to ten days in a freezer, with its structure being solved using single crystal X-ray diffraction. Although first observations were by chance, subsequent attempts to form NMS16 resulted, 20–30% of the time, in a mixture of the single-cation phases NS10 and either MS11, or MS7, depending on the relative humidity and temperature conditions, suggesting NMS16 was not thermodynamically stable (though the authors also considered the possibility that their NMS4 precursor could have decomposed into the single-cation phases prior to use).

However, we observe the presence of NMS16 in both our fast- and slow-freeze experiments. Following fast freezing, the phase initially appears to decrease in proportion down to ∼230 K (Fig. 12), suggesting it may be unstable relative to the other phases at higher temperature, but more thermodynamically favoured at low temperatures. Indeed, its intensity and relative proportion increases with falling temperature down to ∼160 K, whereby it levels off until ∼110 K, below which it steadily increases as the temperature falls. This points to NMS16 being a stable low temperature phase, but with slow nucleation and growth kinetics, perhaps limited by the stability (or metastability) of any precursor phase(s). In this respect NMS4 does not seem to be the necessary precursor, as below 160 K, its intensity and relative proportion is constant (Figs. 11 and 12). Further evidence can be seen in Fig. 7(bottom) for the slow-freeze experiment, NMS16 is not observed until ∼30 days or so after a base temperature of 245 K has been reached and long after the Mg-bearing MS7 has disappeared.

Low temperature mineral transformations are generally thought to occur primarily by dissolution and precipitation reactions (e.g., Cole & Chakraborty, 2001; Putnis, 2009). These reactions can involve a mineral transforming from one phase to another, a mineral maintaining its structure and morphology but altering its elemental composition, or a mineral maintaining its structure and elemental composition but reforming into more stable particles through aggregation and growth (e.g., Ostwald ripening). Collectively, these reactions can lead to element- or nuclide-specific repartitioning between the aqueous and solid phases. While there are many different mineral growth, replacement, and transformation mechanisms that can cause these changes, they are generally thought to occur when a system is at disequilibrium (Putnis, 2009; Yardley, 2009; Putnis & John, 2010; Putnis & Ruiz-Agudo, 2013).

In our experiments, NMS16 was clearly distinguished by the presence of a relatively weak Bragg peak at low angle (3.3° 2θ) in the fast-freeze experiment (see Fig. 14) and a much stronger peak, relatively speaking, at ∼2° 2θ in the slow-freeze experiment (note, this is the (001) reflection and the difference in peak positions is due to the difference in X-ray energy, the *d*-spaces are 14.252 Å and 14.19 Å respectively, consistent with differences in temperature, resolution and measurement geometry for the two experiments). Given what looks like a linearly increasing trend below 160 K for its intensity in the fast-freeze data (Fig. 10), it may be reasonable to speculate that if the sample had been maintained at the base temperature beyond the existing end of the fast-freeze experiment, NMS16 would have become more abundant. Leftwich et al. (2013) conducted powder diffractometry experiments using powdered samples mounted on top a circulating methanol temperature-controlled stage inside a humidity controlled cell, reporting that NMS16 persisted down as far as 150 K. Whether this was the limit of either their apparatus, or of the experimental programme itself is not clear, but is consistent with our results for aqueous precipitation. They also reported that transformation from their NMS4 precursor occurred between 243-263 K, which is also consistent with the formation temperature of 245 K observed in the slow-freeze experiment, albeit with greatly differing timescales – Leftwich et al. observed NMS16 forming within minutes. NMS4 is only a minor component of the precipitate formed during the fast-freeze experiment (Fig. 12), while its presence was not detected in the slow cooling experiment and may indicate, therefore, the presence of an alternative formation pathway.

Using Raman microspectroscopy Vu et al. (2016) investigated Na-Cl-Mg-SO_4-H_2O brines frozen at 0.5 K min^{-1} with varying Na^+:Mg^{2+} ratios of 2.13:1, 1:1 and 0.61:1, representing saturated, equimolar and oxidised-salty solutions respectively. Based on the general positions of Raman features in certain characteristic spectral regions, they concluded that the precipitated phases were most likely hydrated sodium sulphate and chloride phases. Though they were unable to make definitive identifications they attributed the sulphate to NS10 and the chloride to $MgCl_2$ and NaCl. They also reported that these phases persisted down to 100 K. Repeating the measurements using compositions based on Marion et al. (2005), Zolotov & Kargel (2009) and Zolotov (2012) yielded a similar conclusion, even for Na^+:Mg^{2+} of 1:∼2 (i.e. similar to MEOS). Noting the unexpected nature of this result and that forming a sodium sulphate requires two cation atoms compared to magnesium sulphate's one, to explain their results they hypothesised that magnesium sulphates have a significantly higher solubility at low temperature than sodium sulphates. This should make the sodium sulphate phases more likely to precipitate and may also be aided by excess SO_4^{2-} ions producing a common ion effect (Pape, 1981), which could also reduce the solubility of sodium sulphate. Although comparative magnesium and sodium sulphate solubility data at low temperatures are absent, investigations of terrestrial seawater brines have shown that sodium sulphate solubility changes significantly as a function of temperature between 273 and 252 K (Butler et al., 2016). Following on from their results, Vu and colleagues developed a thermodynamic chemical divide model (Johnson et al., 2019) to predict Europan precipitates for an ocean pH<8.4 and their precipitation order, where the phases formed at each successive step are determined by a combination of their solubility and ionic compositions. However, more recent experimental work by the same authors (Vu et al., 2020), combining Raman and X-ray diffraction, showed that the precipitated phases depend on both freezing rate and composition. They also found multiple hydrated salts, not predicted by the chemical models, were frequently encountered in the final solid phase, and flash freezing of diluted brines often produced water ice together with amorphous hydrated Mg salts. Thus, while low temperatures may favour Na-sulphate precipitation, the kinetics related to slower rates of temperature decrease may mean that Mg-sulphate precipitation also becomes favourable. As such, the presence of NMS16 may be more reflective of a slower rate of cooling in both our experiments, rather than overall composition.

The Leftwich et al. (2013) observation of NMS16 was made under "Mars relevant" conditions, making it a candidate phase for detection on that planet. The observation here, however, of NMS16 under Europa relevant conditions suggests NMS16 may in fact be a ubiquitous feature throughout all cold Mg-Na

saline environments.

4.2. Mineral stratification under slow freezing

The velocity at which a salt particle precipitated out of solution will subsequently sink is described by Stokes law,

$$S_v = \frac{2}{9} g r^2 \frac{\Delta\rho}{\eta\Phi} \quad (2)$$

where $\Delta\rho = \rho_{\text{solid}} - \rho_{\text{liquid}}$ is the excess density of the solid particle relative to the solution, g is the gravitational acceleration, η the solution's dynamic viscosity, Φ the particle's form (shape) resistance (e.g. oblate spheroid, rod, disk etc.) and r the radius of a sphere of equal volume ($= \sqrt[3]{\frac{3V}{4\pi}}$, where V is the specific volume of the particle). Assuming spherical particles, where r is the simple radius and $\Phi = 1$, for a given viscosity, those particles with the highest excess density will thus achieve the highest sinking velocity. The densities of the various phases identified in this study are given in Table 1.

For a fixed viscosity medium, assuming no potential mixing mechanisms such as liquid turbulence or convective motion etc., over time the particle depth distribution will become such that lower density particles occupy lesser depths than higher density ones. However, for water slowly approaching its freezing point η increases non-linearly, going, for example, from 1.571×10^{-3} Nsm^{-2} at 4 °C to 1.792×10^{-3} Nsm^{-2} at 0 °C at normal pressure[4] such that the sinking effect may be predominant only in slowly cooling solutions. Salinity increases the viscosity slightly (e.g. 1.67×10^{-3} Nsm^{-2} at 4 °C and 1.89×10^{-3} Nsm^{-2} at 0 °C for terrestrial seawater[5] with 35 g/kg salinity) while also depressing the freezing point temperature. We assume, for the sake of argument, that the effect of MEOS salinity is similar and we ignore the viscosity-reducing effect that increases in pressure would have. In a solution that is freezing by reduction in temperature and therefore becoming increasingly viscous, two basic effects will come into play. Firstly, those phases that precipitate early on at higher temperature will do so in a less viscous medium and therefore sink farthest, in proportion to their densities, before being slowed by increased viscosity at lower temperature. Secondly, depending on the rate of cooling, the effect of excess density could subsequently deplete the locale of the heaviest phases should they precipitate early on. In our slow-freeze long duration experiment, the temperature dependent order of precipitation (Eq. 1 and Fig. 7) is such that MS7 ($\rho = 1.679$ g cm^{-3}) and NS10 ($\rho = 1.465$ g cm^{-1}) precipitate prior to ice, so that under the right cooling conditions MS7 could, relative to NS10, be preferentially lost to the solution that will subsequently become entrapped within the ice. The combination of cooling rate and measurement frequency of the slow-freeze experiment means that from the current data we can not resolve the question of whether MS11 ($\rho = 1.512$ g cm^{-3}) precipitates prior to, simultaneous with, or after ice formation (as perhaps indicated by the fast-freeze data, Fig. 8). If MS11 forms just prior to ice, it too could be preferentially lost by sinking. The Europan sea bed has been predicted to consist of salt beds of pure magnesium sulphate (Kargel et al., 2000; Spaun & Head, 2001) and could be derived from sinking MS7 and MS11. Depending on the heat flux coming from the core, deposited MS11 should subsequently dehydrate to MS7 (Prieto-Ballesteros & Kargel, 2005). However, even if MS11 forms simultaneously with, or even just immediately after the ice, it will still be forming in a lower viscosity brine than NMS16 ($\rho = 1.623$ g cm^{-3}) which forms at a much lower temperature and which, despite its high density, would therefore have less opportunity for sedimentation or fluid transport. As a consequence, this could result in an enhancement of NMS16 at shallow depths within Europa's ice crust.

4.3. Relationship with surface morphologies and the observed non-ice component

In this paper we have investigated the formation of hydrated salt species from Europa's ocean water and the complex nature of the precipitates produced by a rapid-freeze experiment compared to a slow-freeze one. Differences between these could potentially infer likely associations with one, or other, of the various surface features summarised in section 1.2, depending on differences in delivery mechanism and the associated rate of freezing.

However, it is important to note that once delivered to the surface, or near-surface regions, freshly precipitated salts will be subjected to a number of destructive and modifying processes. For example, laboratory experiments have shown that for typical Europan surface temperatures, the activation energies for the removal of H_2O from MS7 and NS10 are such that MS7 should remain hydrated for $\sim10^{11}$ to 10^{14} years, while NS10 will likely dehydrate on a scale of $\sim10^3$ to 10^8 years (McCord et al., 2001).

Europa is also imbedded in an intense radiation environment with its surface continually bombarded by energetic electrons, protons and heavy ions (Paranicas et al., 2009), along with a lesser ($\sim$2%) energy flux of solar UV photons capable of dissociating H_2O. The dominant ionizing particles at the surface are electrons and protons, ranging in energy from $<$10 keV to $>$10 MeV, with average energies in the MeV range and penetration depths in the 100s of μm range. Extremely energetic electrons and bremsstrahlung X-rays will penetrate more deeply, while micrometeoroid impact gardening will simultaneously bury the radiation products while bringing fresh material up from depth.

The radiolytic production/destruction rate is described by the G value, which is the number of molecules produced, or destroyed, per 100 eV of energy absorbed by a substance. For example, CO_2 in H_2O ice is destroyed at a rate G(-CO_2) = 0.55 per 100 eV, while the production of SO_2 from sulphate has a typical value of G(SO_2) = 0.004 (Johnson et al., 2004; these are representative of both anhydrous and hydrated phases since O_2 production - a typical radiolysis product of water - is not observed experimentally, McCord et al., 2001). Although G(SO_2) is relatively small, over geological timescales, freshly exposed sulphates will nevertheless suffer radiation damage.

[4] https://www.engineeringtoolbox.com/water-dynamic-kinematic-viscosity-d_596.html
[5] https://www.engineeringtoolbox.com/sea-water-properties-d_840.html

Gardening models suggest irradiated material could be vertically mixed to depths of up to 10 m (Carlson et al., 2009).

SO_2 was the second compound detected on Europa (Lane et al., 1981), with its 0.28 μm absorption feature being present only on Europa's trailing side. The SO_2 linearly correlates with Europa's hydrate phases (Hendrix et al., 2002, 2008) and is consistent with Europa's radiolytic sulphate cycle whereby newly formed SO_2 is photolytically and radiolytically decomposed (Schriver-Mazzuoli et al., 2003; Moore et al., 2007) with a lifetime of a few years in Europa's top 100 μm (Moore et al., 2007). The decomposition products reform sulphate in a repeating cycle, and a radiolytic equilibrium SO_2 abundance is formed that is sensitive to the total sulphur to water ratio (Moore et al., 2007). Except that uniform outgassing of SO_2 over Europa's surface is ruled out by the absence of SO_2 on the leading side, which suggests, instead, that the major source of Europa's SO_2 could derive from implanted S ions from its neighbouring satellite Io (as originally suggested by Lane et al., 1981, though other endogenous sources such as inclusions, hydrates or clathrates have also been suggested). Io is known to be a source of SO_2, most of which quickly becomes dissociated in Jupiter's magnetosphere, allowing a flow of S and O ions to be delivered to the Europan surface. However, since Jupiter's magnetosphere rotates faster ($\sim$10 hrs) than Europa's orbital period ($\sim$3.6 days) these, and other charged particles, are carried over Europa from its trailing to leading hemisphere as the magnetosphere rotates over its body. Brown & Hand (2013) identified a spectroscopic feature on Europa's trailing hemisphere which they attributed to Mg-sulphate, proposing that while the Mg is endogenous, the S is exogenous with the sulphate being produced by radiolytic processing. Similarly, deposits of sulphuric acid hydrates ($H_2SO_4 \cdot nH_2O$) have been proposed to form on the Europan surface by radiolysis involving exogenous S (Dalton et al. 2013).

Europa's surface is thus a complex dynamic environment subject to many physical processes (e.g. review by Carlson et al., 2009), with highly modified non-ice components derived from both endogenous and exogenous matter. However, because of the differential in implantation rates between the leading and trailing hemispheres only those areas of limited exogenic processing are likely to contain surface materials whose composition provide a closer match to pristine oceanic precipitates (Dalton et al., 2013).

Beneath the surface, however, salt precipitation from freezing Europan cryomagma may play a role in the formation of chaos terrain. Mũnoz-Inglesias et al. (2014) investigated the precipitation of MS7 and MS11 alongside ice and CO_2 gas clathrate hydrate as function of $MgSO_4$ concentration. The volume change associated with the formation of these phases was found to depend on the $MgSO_4$ concentration and could potentially lead to the formation of chaos terrain via the formation of either surface fractures, or collapse, depending on the positive or negative volume change associated with the specific mix of sulphate, ice and clathrate. Presumably, corresponding effects will exist for the MEOS salts, other than MS7 and MS11, identified in the present work. Although clathrates have not yet been detected on Europa, their formation via the introduction of clathrate-forming gases into liquid saline water will remove water from the solution resulting in increased brine concentration. If this was to occur inside an aqueous cryo-magmatic chamber, or sill, within the ice crust, the clathrates would separate from the remaining brine by either sinking or floating, depending on the specific temperature and salinity (Safi et al., 2017) which will be determined by temperature-dependent salt precipitation. If clathrates close to the surface were to dissociate, the very rapid release of gas and large negative change in volume would likely cause fracturing and gravitational collapse and could therefore also be a contributory process to the formation of chaos terrain.

4.4. Implications for life on Europa

Life on Earth often appears to thrive at the edges and interfaces between different environments. These are places of disequilibrium and the surface–ice–ocean system on Europa should represent a prime planetary example of a global interface-environment. However, life is also constrained by access to resources and environmental requirements, such that the geographical distribution of any lifeforms that currently exist (or might have existed in the past) on Europa is likely to be heterogeneous. Lipps & Rieboldt (2005) identified $\sim$15 broad categories of habitat that could be possible on Europa, including locations on the sea floor, water column and within the ice crust itself. Ocean circulation, geological activity and thermal history will have resulted in global salt transport (Travis et al., 2012), such that habitable environments on Europa will likely be predominantly saline in nature.

On Earth, channels and inclusions within sea ice containing liquid brines host a wide range of sympagic organisms (bacteria, microalgae, viruses, fungi, protozoans and metazoans) within a physicochemical environment subject to oscillating gradients in temperature, salinity, pH, dissolved inorganic nutrients, as well as dissolved gas and light signatures (Mock & Thomas, 2005). Osmotic conditions within terrestrial brine channels are controlled by brine salinity and are therefore defined by temperature-dependent salt precipitation (e.g. the precipitation of NS10 below 266.75 K; Butler et al., 2016). Microbes inhabiting brine channels near the upper surface of the ice can experience saline concentrations $>$20% (Kottmeier & Sullivan, 1988; Arrigo & Sullivan, 1992; Mock, 2002), while the onset of ice melt can very quickly expose them to freshwater lenses with 0% salinity (Thomas & Dieckmann, 2002). Although the solar flux at Europa is $\sim$27 times weaker than at Earth, light penetration into the Europan ice crust could be up to a $\sim$few m so could in principle support an analogous ice-brine ecosystem (Martin & McMinn, 2018), where life sustaining nutrients and fuel could be supplied from both the surface (via radiativly formed oxidising molecules, Johnson et al., 2004; Paranicas et al., 2009) and/or sea floor processes (Hand et al., 2009). Periodic reductions in salinity, in keeping with those on Earth, could be provided by the formation of melt water lenses (e.g. Fig. 4). Furthermore, although Europa's surface is both young and active in geological terms, it is likely to remain stable for tens of thousands of years (Greenberg, 2008), providing a

potentially long-lived ecological niche within the ice crust in which the temperature-dependent salt precipitates identified in the slow-freeze experiment could, conceivably, play similar regulatory environment-controlling roles. Although temperatures towards the surface on Europa can reach as low as ∼50-90 K, the lower limit of ∼77 K for microbial activity seen in laboratory cultures on Earth (Junge et al., 2006) falls within this range (although at the lowest temperatures this may represent cell maintainance for survival rather than growth), with warmer conditions existing closer to the ice-ocean interface. As a stable low-temperature phase, with a possible enhancement at shallow depths, the nucleation of NMS16 could prove to be of particular astrobiological significance as an environmental regulator.

The biological pump on Earth is the global mechanism by which organic carbon is delivered to the ocean interior and seafloor via the sinking of particulate organic matter, largely derived from deceased planktonic organisms. Sinking particles often coalesce to form aggregates (the marine snow), which increases their sinking velocity and is largely determined, via Eq. 2, by their size and excess density (Smayda, 1971; De La Rocha & Passow, 2007; though the interplay between aggregate radius and density is not straightforward e.g. Passow & De La Rocha, 2006). On Earth, sinking velocity plays a significant role in (a) the long-term sequestration rate of atmospheric carbon, once it has been fixed by organisms in the photic zone, and (b) the delivery of organic nutrients at depth. Sinking velocity, and therefore achieved depth, is enhanced by the incorporation of mineral ballast materials (Ploug et al., 2008a,b), which have themselves been found to promote coagulation of organic particles (Avnimelech & Troeger, 1982; Beaulieu et al., 2005; Verspagen et al., 2006; Passow et al., 2014). Although calcium carbonate biominerals are a ready source of ballast, the primary non-biogenic source is lithogenic dusts and clays supplied by atmospheric deposition and river inflow, the availability and composition of which vary both locally and globally (as well as historically). Since sulphates (including Mg- and Ca-sulphates) are widely used, albeit as solutes, as flocculant additives in water treatment and various commercial/industrial processes, it is worth speculating as to whether low temperature salt precipitates could assume the role of lithogenic matter and similarly promote the coagulation of any organics released from possible ice-brine habitats on Europa. Of relevance here is the recent discovery of abundant gypsum (CS2) crystals embedded within aggregates of Phaeocystis algae collected throughout the water column, and sea floor, at a depths below 2 km in the ice-covered Arctic Ocean, likely constituting a significant, previously unrecognised, contributor to the biological pump in cold regions (Wollenburg et al., 2018, 2020). The CS2 was shown to have been precipitated within sea ice and subsequently released into the water column during melting. Although CS2 is one of the highest density precipitates, it appears to be only a minor component of our MEOS experiments. Considering how MEOS composition differs to terrestrial sea water, other precipitated phases could potentially play a similar role in the transfer of organic matter within the Europan ocean. Given the weaker gravitational acceleration on Europa, the more dense mixed Na-Mg phases (e.g. NMS4, NMS5 and NMS15 see table 1 and discussion in section 4.1) may be more important, even if less abundant.

The above presupposes that life is already somehow established on Europa, however salts may also have been important in the formation and development of the necessary prebiotic components prior to any potential beginnings of Europan life. On the early Earth the concentration of prebiotic organic compounds in a global ocean was likely to have been extremely low (estimates range from $\sim 4\times10^{-3}$ M to $\sim 4\times10^{-12}$ M, Stribling & Miller, 1987; Lahave & Chang, 1976; Miyakawa et al., 2002) and therefore would have been too dilute for the synthesis of nucleotide bases and amino acids to compete with their decomposition by hydrolysis (Miyakawa et al., 2002). However, the concentration within sea ice brine inclusions becomes orders of magnitude higher, and the water activity within the inclusions so low, that prebiotic molecular polymerization is favoured over hydrolysis (Miyakaw et al., 2002). Although Europa is comparable to the Moon in size, its ocean volume is two to three times that of the Earth's, suggesting probable low organic concentrations, as per the early Earth. This suggests brines within the ice crust could potentially have a similar role to play in building complex biomolecules. In addition, the likely thermal structure of the crust suggests there should be a shallow region (i.e., at a depth of a few kilometres) that is favourable for the polymerization of biomolecules, since at low temperatures the Gibbs energies for biomolecule polymerization become negative, allowing for spontaneous polymerisation (Kimura & Kitadai, 2015). This may be further enhanced by the presence of saline species. Glycine (Gly) polymerisation has been shown (albeit in thermal dehydrating conditions) to be accelerated in the presence of $MgSO_4$ (Kitadai et al., 2011). In these experiments up to 6-mer of Gly polymers were synthesized with a total yield ∼200 times greater in the presence of $MgSO_4$ than from Gly on its own. Mg^{2+} ions have also been found to stabilize nucleic acid duplexes to a greater extent than the same concentration of Na^{+} ions (Williams et al., 1989).

In the context of the *RNA world first* hypothesis for the origin of life, following similar arguments, cold ice-brine environments on Earth may have been an essential low temperature step in the early replication of nucleic acids (Trinks et al., 2005; Price, 2007; Vincent et al., 2004; Feller, 2017) and could play a similar role on Europa. It is well known that minerals can provide solid surfaces for a range of biogenic interactions (Cleaves et al., 2012) and experiments show nucleotide oligomerization can be catalysed, for example, by clay surfaces (Ferris, 2002; Huang & Ferris, 2006). When NaCl or $MgCl_2$ are added, both cause an increase in oligomer length, but by different amounts (Jheeta & Joshi, 2014). This last point could raise the possibility of a potentially different biochemical basis for any life that may have developed on Europa, compared to Earth, based on differences in the available inventory of salt phases. It is interesting to note that the two main precipitates observed in this study are Na- and Mg-sulphate phases of high hydration state, but with MS11∼2×NS10. As discussed in section 4.2, stratification into Na-rich salts near the surface and Mg-rich salts

below could either restrict life-producing biogenic reactions to the near-surface regions, in keeping with Earth's Na-rich hydrosphere, or possibly result in two distinct bio-geochemical near-surface and deep subsurface zones.

4.5. Future work

4.5.1. In situ fast freezing on I11. The freezing rates associated with the various mechanisms for delivering oceanic matter to Europa's surface (section 1.2) likely cover a range that exceeds the rapid- and slow-freezing experiments reported here. In our fast freeze experiment we began cooling the MEOS sample from a starting temperature of 256 K, however, it is possible that employing varying rates of cooling and starting temperatures could result in the freezing in of different molecular liquid arrangements which could influence precipitate formation and subsequent evolution, as potentially could small local deviations in the chemical composition. Mechanisms involving very steep temperature gradients likely also subject their materials to fast, or flash, freezing. For oceanic water erupted by plumes, whose frozen contents return to the surface, the assemblage of salts could be even more complex than those reported here, since water droplets comprising part of a plume are frozen extremely quickly, with loss of about 17% of the water by evaporation and sublimation if the water is originally liquid and at 273 K. The 17% loss of water corresponds to a 20% increase in the concentration of non-volatile solutes (Pasek, 2020).

In the laboratory, flash freezing can be achieved by dropping solutions onto a cold surface, or into liquid nitrogen, and will likely produce a disequilibrium solid whose initial state (i.e. phase structure and amorphicity) will be very different to either the rapid- or slowly-cooled solutions. For example, Fortes (2018) notes that immersion of pure water in liquid nitrogen likely produces stacking disordered ice. This contains a mixture of strained cubic and hexagonal stacking sequences, rather than just the hexagonal sequence produced by "normal" cooling, and is also formed when water is vapour deposited, or frozen extremely fast as submicron-sized droplets. In addition, *ex situ* formation necessarily requires *ex-situ* preparation, which for X-ray powder diffraction means grinding, loading into capillaries, transportation and mounting on the instrument. Under such conditions some degree of relaxation, crystallisation, or phase transformation could occur. Indeed, as Figs. 10 to 12 show, under rapid cooling, significant changes occur within the first one or two temperature steps and may occur even more quickly for a disequilibrium solid formed by flash freezing.

However, the existing beamline set up can be used for *in situ* flash freezing. As Fig. 6 shows, the capillary is normally situated inside the cryostream nozzle. The cryostream is mounted on a separate large motorized xyz table separate to the diffractometer, allowing the cryostream to be pre-set to a chosen temperature and driven over the capillary. Although there may be a small thermal lag due to the thermal conductivity of the capillary, the PSD can be set to collect data before, during and at subsequent times post-freezing, returning data on phase evolution.

Although the current PSD is relatively fast at ∼20 Hz frame rate (Thompson et al., 2011), in normal use it is limited by a combination of data collection count time (two exposures separated by a 0.25° 2θ step), readout speed and network file storage write times, which limit the practical temporal resolution to ∼3-5 s (although this can be improved by using local storage and/or fast triggering at fixed position). At the time of writing, the I11 beamline is undergoing an extensive upgrade programme to the monochromator (completed), diffractometer (completed), source (due late 2021) and detectors (early 2022). The latter will see the existing Mythen-II based PSD replaced with one based on a 2-D tiled design using Mythen-III technology (Andrä et al., 2019). This will eliminate two-position scanning, provide a significant gain in readout speed, lower background noise and shorter dead time at high photon rates, allowing for frame rates in the kHz range for *in situ* flash freezing measurements.

4.5.2. Application to other planetary objects. Many of the icy objects in the outer Solar System are believed to harbour liquid oceans, supported variously by observation, modelling or plausible circumstance (e.g. reviews by Hussmann et al., 2006; Massé et al., 2014; Nimmo & Pappalardo, 2016; see also Table 1 in Thompson et al., 2018). Some of these will be in direct contact with their rocky cores. For example, gravimetric measurements for Enceladus suggest rock-ocean and ice-ocean interfaces at depths of ∼50 km (∼5.3 MPa) and 35-40 km (3.6-4.2 MPa), respectively (Iess et al., 2014), and with pressures well within the range experienced by terrestrial life. For other objects the ocean will be isolated by high- and low-pressure ice phases. For example, Europa's neighbour Ganymede is the largest moon of the Solar System and has a surface containing both old, densely-cratered terrain and widespread tectonically resurfaced (i.e. younger) regions similar to Europa. Its interior has a differentiated structure (Sotin & Tobie, 2004), and is also subject to tidal heating due to resonant-forcing of its orbital eccentricity. However, because of its larger size and higher abundance of water, relative to its denser mantle materials, pressures at the water-rock interface are likely to be as high as 1.2 GPa. Consequently, any liquid ocean will probably be sandwiched between layers of ice I at the surface and ice V and VI at the seabed (Sotin & Tobie, 2004). Such high pressures are likely to close microfractures in the high pressure ice, inhibiting significant water-rock interaction post-differentiation (Vance et al., 2007). This means that the ocean composition will have been determined largely by the extent of the water-rock interaction during its period of differentiation and likely preserved by its subsequent isolation. Due to the high bulk water to rock ratio and reduced hydrogen fugacity caused by the loss of hydrogen to space, primordial water-rock interactions within chondritic parent accretion materials would, in Ganymede's case, have favoured a rise in the solubility of sulphate and Mg^{2+} (King et al., 2004; Zolotov and Kargel, 2009) giving rise to an ocean dominated by $MgSO_4$. The actual salinity of Ganymede's ocean is not known, but could be 3–10% (Vance et al., 2014), while reflectance spectra measured by the Galileo mission suggests the predominant non-ice surface materials are moderately hydrated materials similar to those on Europa, i.e. salts

(McCord et al., 2001).

Beyond the ocean worlds of the Solar System there are over 4000 known exoplanets, many of which have masses and radii comparable to Earth's. Theoretical analysis suggests that somewhere in the region of ∼26% could be ocean worlds (Quick et al., 2020), a proportion of which could reasonably be assumed to be similar to the icy moons of our own Solar System. This is a highly active field of academic research of obvious significance, where observational techniques and analyses are rapidly evolving. Atmospheric spectroscopy of exoplanets is now routinely possible using current observational techniques, instrumentation and existing datasets (e.g. Seager & Deming, 2011; Seager, 2013; Lacour et al., 2019; Tsiaras et al., 2019) and will improve with the next generation of space telescopes (e.g. James Webb Space Telescope scheduled to launch 2021) and future Earth- and space-based instruments currently being designed (e.g. ESA's Atmospheric Remote-sensing Infrared Exoplanet Large-survey - ARIEL - mission due to launch 2028). Atmospheric compositional data from these instruments will feed into climate and planetary models with the expectation of identifying habitable worlds (e.g. Catling et al., 2018; Kaltenegger et al., 2020). For example, the TRAPPIST-1 system comprises seven Earth-sized planets labelled, in order of radial distance, TRAPPIST-1 b through to h. Of these, TRAPPIST-1 e, f and g all orbit within the "habitable zone" where water could potentially exist in liquid form. Current models (Lincowski et al., 2018) suggest TRAPPIST-1 e could host liquid water, while TRAPPIST-1 f and g could potentially be frozen icy worlds, depending on their original water budget. The central star of the TRAPPIST-1 system is an M-type dwarf star. These are smaller than the Sun in both mass and size, but are in fact the most abundant type of star (Henry et al., 2006) with high occurrences in multi-planet systems (Ballard & Johnson, 2016; Gillon et al., 2017) and habitable zone Earth-sized planets (Dressing & Charbonneau, 2015), making the likely existence of icy ocean exo-worlds highly probable.

Given the extremely widespread production from stellar sources, and distribution throughout interstellar space, of silicate- and carbonaceous-based cosmic dust grains as the ultimate precursor planetary material (e.g. Jones, 2007; Blum & Wurm, 2008) it is likely that a chondritic-like rocky core will lie at the heart of exo-ocean worlds and that water-rock interactions will result in the existence of saline exo-oceans.

The geological record shows that the Earth experienced a number of freezing episodes 630-720 MYa, during the Neoproterozoic eon, when extensive glaciation covered much, or all, of the oceans, separating them from the atmosphere and likely resulting in the large-scale extinction of preglacial microorganisms and plants (e.g. revue by Banik, 2016). These Snowball Earth episodes (the Cryogenian) were the result of runaway ice-albedo feedback. The albedo was further increased by an extensive MS10 salt crust in tropical regions formed by the sublimation of sea ice, the MS10 having precipitated within the sea ice once temperatures fell below 150 K (Carns et al., 2015, 2016). It was during the Cryogenian that eukaryote cells first acquired the ability to biosynthesize certain sterols (C_{26}–C_{30}, Hosihno et al., 2017). Synthesis of C_{29} sterols, for example, significantly reduces the temperature dependence of membrane dynamics, extending the temperature range for biological membrane processes. This confers a distinct evolutionary advantage against large temperature fluctuations and likely gave rise to the global dominance of green algae within the marine ecosystem. The fossil record also shows that the end of the Cryogenian coincided with the rise of predation by heterotrophic plankton (van Maldegem et al., 2019). These are marine microbes that rely on gaining energy by the consumption of other organisms (e.g. the green algae). The rise of predation established a food chain and ultimately led to the Cambrian explosion and the development of intricate lifeforms, including the lineages from which all animals, including humans, derive from. Despite the initial extinction, the Cryogenian period was therefore a driver for evolution rather than an inhibitor. The conditions under which an exoplanet orbiting within the habitable zone with liquid water covering a proportion of its surface can enter (and recover from) a snowball phase are a matter of current debate, but will depend on the star's spectral type, the planet's rotational and orbital properties and its's geographical characteristics (e.g. Checlair et al., 2018, 2019; Foley, 2019; Paradise et al., 2019; Walsh et al., 2019; Yue & Yang, 2020), while the development and nature of a salt crust will depend on the details of it's ocean composition. It is worth noting that the abiotic origin of life is arguably the greatest unsolved scientific problem, but thus far has no standard model. Thus, if the role of low-temperature salt precipitates in the origin and development of life (as discussed in section 4.4) turn out to be correct then, icy, or frozen, ocean worlds could represent a universal step in the development of life throughout the universe.

In this paper we have focussed on a single ocean composition based on a chondritic composition; however it needs to be borne in mind that *the* chondritic composition is largely a notional average based on abundances deduced from primitive meteorites, whose localised elemental abundances were determined by those of the solar nebula. It is generally held that the bulk of the matter in the primordial solar nebula was relatively uniform in chemical and isotopic composition (Palme et al., 2014). Furthermore, the elemental composition is roughly similar to that of other stars in the solar neighbourhood. However, there are observed compositional differences among stars at similar evolutionary stages (e.g., dwarf stars). These are not caused by internal properties (i.e. nucleosynthesis), but reflect the variation in the chemical evolution of the Galaxy, whose elemental and isotopic composition has evolved with time (Timmes et al., 1995). Elemental production by nucleosynthesis in successive generations of stars leads to heavy element (i.e. elements beyond C, N and O) enrichment of the interstellar medium over time, such that there is an overall increase in the so-called metallicity of both the Galaxy and newly forming stars, which similarly inherit the elemental abundances present at the place and time they form. Their planets, in turn, inherit the materials left over from the star-forming process, which will have been processed to varying extent during both the stellar formation and planetary build. The process is stochastic on a local scale, but

there is a gradient in the Galaxy with central, denser regions being more chemically evolved (Anders et al., 2017) due to faster star-formation rates. The lifetime of a star is determined by its initial mass, ranging from many billions of years for a M-type star, to only a few million years for stellar masses $\sim 10\times$ greater than an M-type star. A star's orbit within the galactic disk will also tend to wander outwards with time due to the phenomenon of radial migration, which is influenced by past galactic collisions, the number of spiral arms and the size and movement of the central galactic bar (Minchev & Famaey, 2010; Minchev et al., 2018). Since dust production mostly occurs towards the end of a star's life, those that are dying and producing dust at any one time and place may therefore have quite different ages, formation sites and initial compositions. Isotopic analysis of unprocessed inorganic pre-solar grains identified within chondrite meteorites suggest their formation around a number of distinct stellar sources: red giant/asymptotic giant branch (RGB/AGB) stars, supernovae and, possibly, novae and Wolf-Rayet stars (e.g. Leitner et al., 2012; Nguyen et al., 2016). The range in isotopic composition suggests a minimum of 35 to 40 stellar sources contributed to the nebula from which our Sun and Solar System formed (Alexander, 2001), while its birth place was approximately 2000 light years closer in towards the galactic centre (Minchev et al., 2018). Variation and fluctuations in the average chondritic composition over galactic length scales is therefore likely.

It should be clear that ocean worlds, not only those of the Solar System but also the probable subset of the exoplanet population, will likely have oceans that vary to some degree in their compositions, depending on their size (extent of water-rock interaction), specific "chondritic" building block materials and position in their own nebula. This latter point will determine volatile content which could also influence ocean composition. For example, Saturn's moon, Titan, likely formed at a point in the Saturnian sub-nebula where temperatures were below the condensation temperatures of various primordial volatile species, such that concentrated eutectic solutions at temperatures below 273 K would have formed that were typically rich in CH_3OH, NH_3, CO_2 and H_2S (Sohl et al., 2010). Under freezing conditions these would have been further concentrated and capable of facilitating the dissolution of mineral phases and the chemical reactions necessary to yield a saline ocean. In particular, the interaction of ammonia-rich liquids with magnesium sulphate, contained within chondritic core materials, could result in an ocean enriched in ammonium sulphate (Fortes et al., 2007) rather than magnesium sulphate or sodium chloride. In exoplanetary systems, Titan-like planets could prove to be highly abundant since Titan's effective temperature corresponds to that experienced by a body orbiting at 1 AU (Earth-Sun distance) around a late M-type dwarf star. Much, therefore, could be gained by applying the *in situ* experimental procedures, high resolution time and temperature resolved synchrotron X-ray diffraction measurements and crystallographic analysis of the present work to a systematic range of ocean compositions.

4.5.3. Organic-inorganic interactions. Finally, work has also begun on using the apparatus and procedures described here to investigate the role and behaviour of organics in precipitating brines. Amino acids, for example, are highly soluble and can be crystallised from aqueous solutions. They are also a well-documented constituent of primitive carbonaceous chondrite meteorites and constitute a major organic component of the insoluble macromolecular material contained within these objects, reflecting the diversity of conditions that existed on their original parent bodies (Elsila et al., 2016). The most abundant amino acid across all meteorites is Gly, which has also been identified in samples returned from comet 81P/Wild 2 by NASA's STARDUST mission (Elsila et al., 2009), its cometary origin being confirmed by ^{13}C isotope signature. Gly has subsequently also been detected in the coma of 67P/Churyumov-Gerasimenko by the ROSINA mass spectrometer on the Rosetta Orbiter (Altwegg et al., 2016), while Gly precursor molecules have been identified in the astronomical spectra of many other comets including Halley, Hyakutake, Tempel-1, Giacobini-Zinner, Hartley 2 and Hale-Bopp. Hypervelocity impact experiments using precursor molecules within ice targets have also produced a range of amino acids, with Gly being the most abundant (Martins et al., 2013). The likely presence of amino acids, and Gly in particular, on ice-ocean bodies (including the early Earth) is thus widely acknowledged, and would have arisen either as part of the original chondritic core, delivery via meteorites and impacts from asteroids (meteorite parent bodies) or comets, or indeed via *in situ* synthesis during impact.

Gly has three ambient pressure polymorphs (α-form, $P2_1/n$; β-form, $P2_1$; γ-form,P_2), all of which can be crystallized from aqueous solutions (Surovtsev et al., 2012). As with mineral phases, polymorph crystallisation is a result of the complex interplay between kinetic and thermodynamic factors, i.e. the nucleation rate, the overall rate of crystal growth and the difference in the growth of different crystal faces. Studies of the crystallization outcomes in confined environments, at special surfaces, spray-drying, flash freezing or on adding antisolvent (acetone, ethanol, methanol etc.) have been shown to preferentially select one or other Gly polymorph (Surovtsev et al., 2012). Additionally, flash freezing of aqueous Gly solutions produces an amorphous phase, which transforms on heating to a fourth intermediary phase, prior to forming β-Gly. To our knowledge no systematic studies of Gly crystallisation in freezing saline environments have been performed and, since Gly is capable of incorporating into inorganic hydrated mineral structures (Kavitha & Mahadevan, 2013), such studies could provide new insights into the nature and origin of the non-ice surface mineralogy of icy bodies as well as the early prebiotic stages involved in the origin of life as discussed in section 4.4.

5. Conclusions

Europa has several parallels with Earth in that it is differentiated, has tectonic activity and liquid water in the form of a global saline ocean. Although the ocean is covered by a relatively thick ice crust various physical mechanisms, possibly acting at different times in the moon's geologically recent history, are likely to have delivered significant quantities of

oceanic matter to the surface, resulting in the presence of hydrated salt deposits. We have conducted experiments to identify the types of salts that may form and be present on the surface by investigating low temperature precipitation from a model Europan ocean solution (MEOS) of chondritic composition under two freezing regimes. Under ultra slow freezing, the order of precipitation generally follows that predicted by equilibrium thermodynamics, with the exception that after a significant length of time at low temperature we observe the formation of a highly hydrated sodium-magnesium sulphate phase ($Na_2Mg(SO_4)_2{\cdot}16H_2O$), whose identification and structure have only been reported in recent years. Under fast freezing conditions on the other hand, all possible phases appear to precipitate at the same time (within the time and temperature resolution of our experiment), but then, with falling temperature undergo an initial chaotic-like adjustment in their intensities and relative proportions, no doubt due to the initial assemblage being a disequilibrium one. However, below $\sim$150 K the system appears to settle with subsequent changes in both their intensities and relative proportions progressing more smoothly. We were able to group the precipitates according to whether their abundances increased, decreased or remained essentially constant. The two main phases were meridianiite ($MgSO_4{\cdot}11H_2O$) and mirabilite ($Na_2SO_4{\cdot}10H_2O$). The $Na_2Mg(SO_4)_2{\cdot}16H_2O$ phase was also observed in the fast freezing experiment and was one of the phases found to increase in abundance with decreasing temperature. Based on the increased sinking velocity of dense phases at higher temperatures, we have proposed a mechanism by which the abundance of $Na_2Mg(SO_4)_2{\cdot}16H_2O$ could be enhanced at shallow depths within Europa's ice crust.

The precipitation of salts on Europa parallels the precipitation of salts from polar sea ice on Earth and which in turn play an important ecological role in regulating the habitability of such environments. Since conditions on Europa are widely considered suitable for life we have discussed the possible biological role that salt precipitates could play on Europa. However, ocean salts on Earth are dominated by sodium chloride, while the salts produced from our model solution are sodium and magnesium sulphates and could lead to significant potential geo-biochemical differences. Although we have concentrated on a single instance of a possible Europan ocean composition, we have discussed how the techniques and methodology of the current work could be applied to further our understanding not only of other solar system bodies but also those exoplanets currently being discovered that also likely host icy oceans.

The identification of materials on planetary surfaces via spectral fitting is limited by the library of plausible candidate materials available with which to do the fitting. As such, laboratory experiments, such the ones described here, are invaluable in providing clues and constraints, since formed phases are determined by nature rather than theory. The observation of $Na_2Mg(SO_4)_2{\cdot}16H_2O$ is a prime example. Its existence was discovered rather than predicted and, to the best of our knowledge, has not previously been suggested as a candidate phase for Europa. Indeed for disequilibrium systems, such as rapid or flash freezing, thermodynamic modelling is likely to be wholly inadequate, leaving laboratory experimentation as the only way forward. Added to this is the surprising complexity of the sulphate and sulphate-chloride systems, particularly at low temperatures where a wide range of hydration states with multiple pathways between them can exist. The discovery of new phases such as $Na_2Mg(SO_4)_2{\cdot}16H_2O$ in recent times suggests there may yet be further discoveries to be made.

Acknowledgements

This work was supported by Diamond Light Source LDE beamtime award EE10025. The authors thank Mr Jonathan Potter for his assistance in maintaining the cold cell. BMB was supported by a NERC Algorithm Studentship (NE/K501013) and a Macaulay Development Trust Fellowship (MDT-50). ES acknowledges Diamond Light Source and Keele University for financial support.

References

Addadi, L., Raz, S, Weiner, S. (2003). *Adv. Mater.* **15**, 959–970.
Alexander, C. M. O'D. (2001). *Phil. Trans. R. Soc. Lond. A*, **359**, 1973–1989.
Altwegg, K. Balsiger, H, Bar-Bun, A. and 29 others (2016). *Science Advances*, **2** e1600285.
Anders, F., Chiappini, C., Minchev, I. and 21 others. (2017). *Astron. Astrophys.* **600**, A70(1–6).
Andrä, M., Barten, R., Bergamaschi, A., Brückner, M., Casati, N., Cervellino, A., Chiriotti, S., Dinapoli, R., Fröjdh, E., Greiffenberg, D. and Lopez-Cuenca, C. (2019). *J. Instrumentation*, **14(11)**, p.C11028.
Arrigo, K. R., Sullivan, C. W. (1992). *J. Phycol.* **28**, 746–756.
Avnimelech, Y., Troeger, B. (1982). *Science*, **216**, 63–65.
Ballard, S., Johnson, J. A. (2016). *Astrophys. J.*, **816**, 66(9pp).
Banik, I. (2016). *Astrobiol. Outreach*, **4**, 153(18pp).
Baross, J. A., Hoffman, S. E. (1985). *Origins Life*, **15**, 327–345.
Beaulieu, S. E., Sengo, M. R. Anderson, D. M. (2005). *Harmful Algae*, **4**, 123–138.
Bills B.G. et al. (2009). In *Europa* R. Pappalardo, W.B. McKinnon, K. Khurana (Eds.), University of Arizona Press, Tucson.
Blum, J., Wurm, G. (2008). *Annu. Rev. Astron. Astrophys.* **46**, 21–56.
Bots, P., Benning, L. G., Rodriguez-Blanco, J.-D., Roccal-Herrero, T., Shaw, S. (1012). *Cryst. Growth Des.* **12**, 3806–3814.
Brown, M. E. & K. P. Hand (2013). *Astron. J.* **145**(4), 110(1–7).
Brown, M. E., Hill, R. E. (1996). *Nature*, **380**, 229–231.
Butler, B. M., Papadimitriou, S., Santoro, A., Kennedy, H. (2016). *Geochim. Cosmochim. Acta*, **182**, 40–54.
Carlson, R. W., W. M. Calvin, J. B. Dalton III, G. B. Hansen, R. L. Hudson, R. E. Johnson, T. B. McCord, & M. H. Moore (2009), in Europa, Eds. R. T. Pappalardo, W. B. McKinnon, & K. K. Khurana, pp. 283–327, Univ. of Ariz. Press, Tucson.
Carns, R. C., Brandt, R. E., Warren, S. G. (2015). **J. Geophys. Res. Oceans**, **120** 7400–7412
Carns, R. C., Light, B., Warren, S. G. (2016). *J. Geophys. Res. Oceans*, **121**, 5217–5230.
Catling, D. C., Krissansen-Totton, J., Kiang, N. Y. and 7 others (2018). *Astrobiol.* **18**, 709-738.
Checlair, J. H., Menou, K., Abbot, D. S. (2017). *Astrophys. J.* **845**, 132(10pp).
Checlair, J. H., Salazar, A. M., Paradise, A., Menou, K., Abbot, D. S., (2019). *Ap. J. Lett.* **887**, L3(5pp).
Cleaves II, H. J., Scott, A. M., Hill, F. C., Leszczynski, J., Sahai, N. & Hazen, R. (2012). *Chem. Soc. Rev.* **41**, 5502–5525.
Combes, C., Rey, C. (2010). *Acta Biomaterialia*, **6**, 3362–3378.
Corliss, J. B., Baross, F. A., Hoffman, S. E. (1981). *Oceanologica Acta*, **SP. Proc. 26th Int. Geol. Cong.** 59–69

Craft, K.L. et al., (2016). *Icarus*, **274**, 297–313.

Dalton. J. B. (2012). *J. Geophys. Res.* **17**, E09001

Dalton, J. B., Prieto-Ballesteros, O., Kargel, J. S., Quinn, R. (2005). *Icarus*, **177**, 472–490.

Dalton, J. B., Cassidy, T., Paranicas, C., Shirley, J. H., Prockter, L. M., Kampm L. W. (2013). *Planet. Space Sci.* **77**, 45-63.

De La Rocha, C. L. N., Passow, U. (2007). *Deep-Sea Res. II*, **54**, 639–658.

Doggett, T., Greeley, R., Figueredo, P. (2009). In Europa, Eds Pappalardo, R. T., McKinnon, W. B., Khurana. University of Arizona Press, Tucson, pp. 137–159.

Dombard, A.J., Patterson, G. W., Lederer, A.P., Prockte,r L.M. (2013). *Icarus*, **223**, 74–81.

Dressing, C. D., Charbonneau, D. (2015). *Astrophys. J.* **807**, 45(23pp)

Elsila, J. E., Glavin, D. P., Dworkin, J. P. (2009). *Meteorit. Planet. Sci.* **44**, 1323–1330.

Elsila, J. E., Aponte, J. C., Blackmond, D. G., Burton, A. S., Dworkin, J. P., Glavin, D. P. (2016). *ACS Central Science*, **2**, 370–379.

Fagents, S. A. (2003). *J. Geophys. Res.* **108**(E12), 5139(1-18).

Fagents, S. A., Greely, R. and the Galileo SSI Team (1997). *Lun. Planet. Sci. conf. ser.* **XXVIII**, 1196.

Fanale, F. P. Li, Y. H., Decarlo, E., Domergue-Schmidt, N., Sharma, S. K., Horton, K., Granahan, J. C. and the Galileo NIMS Team, (1998). *Lun. Planet. Sci. conf. ser.* **XXIX**, 1248.

Fanale, F. P., Li, Y.-H., De Carlo, E. Farley, C., Sharma, S. K., Horton, K., Granahan, J. C. (2001). *J. Geophys. res.* **106**(7), 14595–14600.

Feller, G. (2017). *life*, **7**, 25(2-9).

Ferris (2002). *Orig. Life Evol. Biospheres*, **32**, 311-332.

Figueredo, P. H., Greeley, R. (2000). *J. Geophys. Res. Planets*, **105**, 22629–22646.

Foley, B. J. (2019). *Astrophys. J.* **875**, 72(20pp).

Fortes A. D., Grindrod P. M., Trickett S. K. and Vočadlo L. (2007). *Icarus*, **188**, 139–153.

Fortes, A. D. (2018). *Acta Cryst. B*, **74**, 196–216.

Galley, R. J., Else, B. G. T., Geilfus, N. -X., Hare, A. A., Isleifson, D., Barber, D. G., Rysgaard, S. (2015). *Cold Regions Sci. Technol.* **111**, 39–48.

Gillon, M., Triaud, A. H. M. J., Demory, B.-O., et al., (2017). *Nature*, **542**, 456–460

Greeley, R., Figueredo, P. H., Williams, D. A., Chuang, F. C., Klemaszewski, J. E., Kadel, S. D., Prockter, L. M., Pappalardo, R. T., Head, J. W., Collins, G. C., Spaun, N. A., Sullivan, R. J., Moore, J. M., Senske, D. A., Tufts, B. R., Johnson, T. V, Belton, M. J. S., Tanaka, K. L., (2000). *J. Geophys. Res. Planets*, **105**, 22559–22578.

Greenberg, R. (2008). *Unmasking Europa, the search for life on Jupiter's ocean moon.* Springer, New York

Greenberg, R., Geissler, P., Hoppa, G., Tufts, B. R., Durda, D. D., Pappalardo, R. T., Head, J. W., Greeley, R., Sullivan, R., Carr, M. H. (1998). *Icarus*, **135**, 64–78.

Greenberg, R., Hoppa, G., Tufts, B. R., Geissler, P., Riley, J., Kadel, S. D. (1999). *Icarus*, **141**, 263–286.

Günther, C., Becker, A., Wolf, G., Epple, M. (2005). *Z. Anorg. Allg. Chem.* **631**, 2830–2835.

Hand, K. P., Chyba, C. F. (2007). *Icarus*, **189**, 424–438.

Hand, K. P., Chyba, C. F., Priscu, J. C., Carlson, R. W., Nealson, K. H. (2009). In *Europa*. R. Pappalardo, W.B. McKinnon, K. Khurana (Eds.), Univ. of Arizona Press, Tucson, pp. 589-630.

Hazel, R., Meersman, F., Ono, F., MacMillan, P. F. (2016). *Life*, **6**, 34(1–8).

Hendrix, A. R., Carlson, R. W., Mehlman, R., Smythe, W. D. (2002). In Jupiter after Galileo and Cassini, p. 108. Observatorio Astronomico de Lisboa, Lisbon.

Hendrix, A. R., Carlson, R. W., Johnson R. E. (2008). *Bull. Am. Astron. Soc.* **40**, Abstract No. 59.07.

Henin, B. (2018). *Exploring the ocean worlds of our solar system.* Spinger (Switzerland).

Head, J. W., Pappalardo, R. T. (1999). *J. Geophys. Res.* **104**, 27143-27155.

Head, J. W., Pappalardo, R. T., Sullivan, R. (1999). *J. Geophys. Res.* **104**, 24223–24236.

Henry, T. J., Jao, W.-C., Subasavage, J. P., Beaulieu, T. D., Ianna, P. A., Costa, E., Mndez, R. A. (2006), *Astron. J.* **132**, 2360–2371.

Holm, N. G. (1992). *Origins Life Evol. Biosphere*, **22**, 5–14.

Horst, S. M., Brown, M. E. (2013). *Astrophys. J. Lett.* **764**, L28.

Hoshino, Y., Poshibaeva, A., Meredith, W. and 18 others (2017). *Sci. Adv.* **3**, e1700887(7pp).

Huang, W., Ferris, J. P. (2006). *J. Am. Chem. Soc.* **128**, 8914–8919.

Hussmann, H., Spohn, T. (2004). *Icarus*, **171**, 391–410.

Hussmann, H., Sohl, F., Spohn, T. (2006). *Icarus*, **185** 258–273.

Iess, L., Stevenson, D. J., Parisi, M., Hemingway, D., Jacobson, R. A., Lunine, J. I., Nimmo, F., Armstrong, J. W., Asmar, S. W., Ducci, M., Tortora, P. (2014). *Science*, **344**, 78–80.

Jheeta, S., Joshi, P. C. (2014). *Life*, **4**, 318-330.

Jia, X., Kivelson, M. G., Khurana, K. K., Kurth, W. S. (2018). *Nat. Astron.* **2**, 459–464.

Jones, A. (2007). *Eur. J. Mineral.* **19**, 771–782.

Johnson, R. E., Carlson, R. W., Cooper, J. F., Paranicas, C., Moore, M. H., Wong, M. C. (2004). In Jupiter: The Planet, Satellites and Magnetosphere, Cambridge planetary science, Vol. 1, Cambridge, UK: Cambridge University Press, pp.485-512.

Johnson, P. V., Hodyss, R., Vi, T. H., Choukroun, M. (2019). *Icarus*, **321**, 857–865.

Johnston, S. A., Montesi, L. G. J. (2014). *Icarus*, **237**, 190–201.

Junge, K., Eicken, H., Swanson, B. D., Deming, J. W. (2006). *Cryobiology*, **52**, 417-429.

Kadel, S. D., agents, S. A., Greeley, R., Galileo SSI Team, (1998). *Lunar Planet. Sci. Conf. Ser.* **XXIX**, 1078

Kaltenegger, L., MacDonald, R. J., Kozakis, T., Lewis, N. K., mamajek, McDowell, J. C., Venderburg, A. (2020). *Astrophys. J. Lett.* **901**, L1(9pp).

Kargel, J. S. (1991). *Icarus*, **94**, 368–390.

Kargel, J. S., Kaye, J., Head III, J. W., Marion, G. M., Sassen, R., Crowley, J., Prieto, O., Grant, S. A., & Hogenboom, D. (2000). *Icarus*, **148**, 226–265.

Kashchiev, D. and van Rosmalen, G. M. (2003). *Cryst. Res. Technol.* **38**, 555–574.

Kattenhorn, S. A. (2002). *Icarus*, **157**, 490–506.

Kattenhorn, S. A., Prockter, L. M. (2014). *Nature Geoscience*, **7**, 762–767.

Kavitha, Mahadevan (2013). *IOSR J. Appl. Phys.* **5**, 45–53.

Kempe, S., Kazmierczak, J. (2002). *Astrobiology*, **2**, 123–130.

Khurana, K. K., Kivelson, M. G., Hand, K. P., Russell, C. T. (2009). In *Europa*. R. Pappalardo, W.B. McKinnon, K. Khurana (Eds.), University of Arizona Press, Tucson, pp. 571–588.

King, P. L., Lescinsky, D. T., Nesnitt, H. W. (2004). *Geochim. Cosmochim. Acta*, **68**, 4993–5008.

Kimura, J., Kitadai, N. (2015). *Astrobiology*, **15**, 430–441.

Kitadai, N., Yokoyama, T., Nakashima, S. (2011). *Geochim. Cosmochim. Acta*, **75**, 6285–6299.

Kottmeier, S. T., Sullivan, C. W. (1988). *Polar Biol.* **8**, 293–304.

Kuskov, O. L., Kronrod, V. A. (2005). *Icarus*, **177**, 550–569.

Lacour, S., Nowak, M., Wang, J. and 85 others (2019). *Astron. Astrophys.* **623**, L11(1–6).

Lahave N., Chang S. (1976). *J. Mol. Evol.* **8**, 357–380.

Lane, A. L., Nelson, R. M., Matson, D. L. (1981). *Nature*, **292**, 38–39.

Leftwich, K. M., Bish, D. L., Chen, C. H. (2013). *Amer. Miner.* **98**, 1772–1778.

Leitner, J., Vollmer, C., Hoppe, P., Zipfel, J. (2012). *Astrophys. J.* **745**, 38(16pp).

Lincowski, A. P., Meadows, V. S., Crisp, D., Robinson, T. D., Luger, R., Listig-Yaeger, J., Arney, G. N. (2018). *Astrophys. J.* **867**, 76(34pp).

Linley, T. D., Gerringer, M. E., Yancey, P. H., Drazen, J. C., Weinstock, C. L., Jamieson, A. J. (2016). *Deep Sea Res. Pt. I* **114**, 99–110.

Lipps, J. H., Rieboldt, S. (2005). *Icarus*, **177**, 515–527.

Leonard, E. J., Yin, A., Pappalardo, R. T., Patthoft, D. A., Schenk, P., Prockter, L. M. (2015). *Lun. Planet. Sci. Conf. Ser.* **46**, 2429.

Leonard, E. J., Pappalardo, R. T., Yin, A. (2018). *Icarus*, **312**, 100–120.

Lunine, J. I. (2010). *Faraday Discuss.* **147**, 405–418.

Lunine, J. I. (2017). *Acta Astronautica*, **131**, 123–130.

van Maldegem, L. M., Sansjofre, P., Weijers, J. W. H. and 16 others (2019). *Nature Communications*, **10(1)**, 476(pp1-11).

Manga, M., Michaut, C. (2017). *Icarus*, **286**, 261–269.

Mann, A. (2017). *Pub. Nat. Acad. Sci.*, **114**, 4566–4568.

Marion, G. M. (2001). *Geochim. Cosmochim. Acta*, **65**, 1883–1896.

Marion, G. M. (2002). *Geochim. Cosmochim. Acta*, **66**, 2499–2516.

Marion, G. M., Fritsen, C. H., Eicken, H., Payne, M. C. (2003). *Astrobiology*, **3**, 785–811.

Marion, G. M., Kargel, J. S., Catling, D. C., Jakubowski, S. D. (2005). *Geochim. Cosmochim. Acta*, **69**, 259–274.

Massé, M., Beck, P., Schmitt, B., Pommerol, A., McEwan, A., Chevrier, V., Brissaud, O. & Séjourné, A. (2014). *Planet. Space Sci.* **92**, 136–149.

Martin, W.,M., Baross, J., Kelley, D., Russell, M. J. (2008). *Nature Rev. Micobiol.* **6** 805–814.

Martin, A., McMinn, A. (2018). *Int. J. Astrobiol.* **17**, 1–16.

Martins et al. (2013). *Nature Geoscience*, **6**, 1045–1049.

McCord, T. B., Hansen, G. B., Hibbitts, C. A., (2001). *Science*, **292**, 1523–1525.

McCord, T. B., Teeter, G., Hansen, G. B., Sieger, M. T., orlando, T. M. (2002). *J. Geophys. Res.* **107**, E4, 5004(1-6).

McSween Jr., H. Y. (1979). *Rev. Geophys.* **17**, 1059–1078.

Miyakawa, S., Joshi, P. C., Gaffey, M., Gonzalez-Toril, E., Hyland, C., Ross, T., Rybij, K, Ferris, J. (2006). *Orig. Life Evol. Biosph.* **36**, 343–361.

Minchev, I., Famaey, B.(2010). *Astrophys. J.* **722**, 112–121.

Minchev, I., Anders, F., Recio-Blanco, A. and 17 others. (2018). *Mon. Not. Roy. Astron. Soc.* **481**, 1645–1657.

Mock, T. (2002). *Hydrobiology*, **470**, 127–132.

Mock, T., Thomas, D. N. (2005). *Environ. Microbiol.* **7**, 605–619.

Moore, M. H., Hudson, R. L., Carlson, R. W. (2007). *Icarus*, **189**, 409–423.

Mùnoz-Inglesias, V., prieto-Ballesteros, O., Bonales, L. J. (2014). *Geochim. Cosmochim. Acta*, **125**, 466–475.

Murray, C. A., Potter, J., Day, S. J., Baker, A. R., Thompson, S. P., Kelly, J., Morris, C. G., Yang, S. & Tang, C. C. (2017). *J. Appl. Cryst.* **50**, 172-183.

Nguyen, A. N. Keller, L. P., Messenger, S. (2016). *Astrophys. J.* **818**, 51(17pp).

Nimmo, F., Gaidos, E. (2002). *J. Geophys.Res. Planets*, **107(E4)**, 5-1.

Nimmo, F., Pappalardo, R. T. (2016) *J. Geophys. Res. Planets*, **121**, 1378–1399.

Nimmo, F., Manga, M. (2009). In *Europa*, R. Pappalardo, W.B. McKinnon, K. Khurana (Eds.) University of Arizona Press, Tucson, pp. 381–404.

Nunoura, T., Takaki, Y., Hirai, M., Shimamura, S., Makabe, A., Koide, O., Kikuchi, T., Miyazaki, J., Koba, K., Yoshida, N., Sunamura, M., Takai, K. (2015). *Proc. Nat. Acad. Sci.* **112**, E1230-E1236.

Nunoura, T., Nishizawa, M., Hirai, M., Shimamura, S., Harnvoravongchai, P., Koide, O., Morono, Y., Fukui, T., Inagaki, F., Miyazaki, J., Takaki, Y., Takai, K. (2018). *Microbes and Environments*, **33**. 186–194.

Palme H., Lodders K., Jones A. (2014). In Treatise on geochemistry (2nd edition), volume 2. Holland H.D. and Turekian K.K. (eds) . Elsevier (Oxford), p15–36.

Papadimitriou, S., Kennedy, H., Kennedy, P. and Thomas, D. N. (2013). *Geochim. Cosmochim. Acta*, **109**, 241–253.

Paradise, A., Menou, K., Valencia, D., Lee, C. (2019). *J. Geophys. Res.: Planets*, **124**, 2087–2100.

Paranicas, C., Cooper, J. F., Garrett, H. B., Johnson, R. E., Sturner, S. J. (2009). in *Europa*. R. Pappalardo, W.B. McKinnon, K. Khurana (Eds.) University of Arizona Press, Tucson, pp. 529-544.

Pasek, M., A. (2020). *Front. Astron. Space Sci.* **7**, 14(pp7).

Passow, U., De La Rocha, C. L. (2006). *Global Biogeochemical Cycles*, **20**, GB1013.

Passow, U., De La Rocha, C. L., Fairfield, C., Schmidt, K. (2014). *Limnol. Oceanogr.* **59**, 532–547.

Perovich, D. K., & Gow, A. J. (1996). *J. Geophys. Res. Oceans*, **101**, 18327–18343.

Ploug, H., Iversen, M. H., Fischer, G. (2008a). *Limnol. Oceanogr.* **53**, 1878–1886.

Ploug, H., Iversen, M. H., Koski, M., Buitenhuis E. T. (2008b). *Limnol. Oceanogr.* **53**, 469–476.

Postberg, F., Kempf, S., Schmidt, J., et al. (2009). *Nature*, **459**, 1098–1101.

Postberg, F., Schmitt, J., Hillier, J., Kempf, S., Srama, R. (2011). *Nature*, **474**, 620–622.

Prieto-Ballesteros, O., Kargel, J. S. (2005). *Icarus*, **173**, 212–221.

Priscu, J. C., Hand, K. P. (2012). *Microbe*, **7**, 167–172.

Price, P. B. (2007). *FEMS Microbiol. Ecol.* **59**, 217–231.

Priede, I. G., Froese, R. (2013). *J. Fish Biol.* **83**, 1528–1550.

Quick, L. C., Marsh, B. D. (2015). *Icarus*, **253**, 16–24.

Quick, L. C., Roberge, A., Milinar, A. B., Hedman, M. M. (2020). *Pub. Astr. Soc. Pac.* **132**, 084402.

Roth, L., Saur, J., Retherford, K. D., Strobel, D. F., Feldman, P. D., McGrath, M. A., Nimmo, F. (2014a). *Science*, **343**, 171–174.

Roth, L., Retherford, K. D., Saur, J., Strobel, D. F., Feldman, P. D., McGrath, M. A., Nimmo, F. (2014b). *Pub. Nat. Acad. Sci.* **111**, E5123–E5132.

Safi, E., Thompson, S. P., Evans, A., day, S. J., Murray, C. A., Parker, J. E., Baker, A. R., Oliveira, J. M., van Loon, J. Th. (2017). *Astron. Astrophys.* **600**, A88(1–9).

Schmidt, B. E., Blankenship, D. D., Patterson, G. W., Schenk, P. M. (2011). *Nature*, **479**, 502–505.

Schubert, G., Sohl, F., Hussmann, H. (2009). In *Europa*, R. Pappalardo, W.B. McKinnon, K. Khurana (Eds.) University of Arizona Press, Tucson, pp. 353–368.

Schenk, P. M., Pappalardo, R. T. (2004). *Geophys Res. Lett.* **31**, L16703.

Schenk, P. M. (2002). *Nature*, **417**, 419–421.

Schenk, P. M. (2009). *Geophys. Res. Lett.* **36**, L15204.

Schriver-Mazzuoli, L., Schriver, A., Chaabouni, H. (2003). *Can. J. Phys.* **81**, 301–309.

Seager, S. (2013). *Science*, **340**, 577–581.

Seager, S., Deming, D. (2011). *Annu. Rev. Astron. Astrophys.* **48**, 631–672.

Sklute, E. C., Rogers, A. D., Gregerson, J. C., Jensen, H. B., Reeder, R. j., Dyar, M. D. (2018). *Icarus*, **302**, 285–295.

Smayda, T. (1971). *Mar. Geol.* **11**. 105–122.

Sohl, F., Choukroun, M., kargel, J., Kimura, Pappalardo, R., Vance, Zolotov, M. (2010). *Space Sci. Rev.* **153**, 485–510.

Sotin, C., Tobie, G. (2004). *Comptes Rendus Physique*, **5(7)**, 769–780.

Sotin, C., Tobie, G., Wahr, J., McKinnon, W. B. (2009). In *Europa*, R. Pappalardo, W.B. McKinnon, K. Khurana (Eds.) University of Arizona Press, Tucson, pp. 85–118.

Sparks, W. B., Hand, K. P., McGrath, M. A., Bergeron, E., Cracraft, M., Deustua, S. E. (2016). *Astrophys. J.* **829**, 121–142.

Sparks, W. B., Schmidt, B. E., McGrath, M. A., Hand, K. P., Spencer, J. R., Cracraft, M., Deustua, S. E. (2017). *Astron. J. Lett.* **839**, L18(1–5).

Spaun, N. A., Head III, J.W., (2001). *J. Geophys. Res.: Planets*, **106(E4)**, 7567–7576.

Stawski, T. M., besselink, R., Chatzipanagisad, K., Hoevelmann, J., Benning, L. G., Van Driessche, E. S. (2020). *J. Phys. Chem. C*, **124**, 8411–8422.

Stribling R., Miller S. L. (1987). *Orig. Life Evol. Biosph.* **17**, 261–273.

Surovtsev, N. N., Adichtchev, S. V., Malinovsky, V. K., Ogienko, A. G., Drebushchak, V. A., Manakov, A. Yu., Ancharov, A. I., Yunoshev, A. S., Boldyteva, E. V. (2012) *J. Chem. Phys.* **137**, 065103.
Takami, H., Inoue, A., Fujii, F., Horikoshi, K. (1997). *FEMS Microbiol. Lett.* **152**, 279–285.
Tarn, J., Peoples, L. M., Hardy, K., Cameron, J., Bartlett, D. H. (2016). *Frontiers in Microbiology*, **7**, 665(1–15).
Thomas, D. N., Dieckmann, G. S. (2002). *Science* **295**, 641–644.
Thompson, S. P., Kennedy, H., Day, S. J., Baker, A. R., Butler, B. M., Safi, E., Kelly, J., Male, A., Potter, J., Cobb, T., Murray, C. A., Tang, C. C., Evans, A., Mercado, R. (2018). *J. Appl. Cryst.* **51**, 1197-1210.
Thompson, S. P., Parker, J. E.,Marchal, J., Potter, J., Birt, A., Yuan, F., Fearn, R. D., Lennie, A. R., Street, S. R. & Tang, C. C. (2011). *J. Synchrotron Rad.* **18**, 637-648.
Thompson, S. P., Parker, J. E., Potter, J., Hill, T. P., Birt, A., Cobb, T. M., Yuan, F. & Tang, C. C. (2009). *Rev. Sci. Instrum.* **80**, 075107.
Timmes, F. X., Woosley, S. E., Weaver, T. A. (1995). *Astrophys. J. Suppl.* **98**, 617–658.
Travis, B. J., Palguta, J., Schubert, G. (2012). *Icarus*, **218**, 1006–1019.
Trinks, H., Schröder, W., Biebricher, C. K. (2005). *Orig. Life Evol. Biosph.* **35**, 429–445.
Tsiaras, A., Waldmann, I. P., Tinetti, G., Tennyson, J., Yurchenko, S. N. (2019). *Nature Astron.* **3**, 1086–1091.
Vance, S., Bouffard, M., Choukroun, Sotin, C. (2014). *Planet. Space Sci.* **96**, 62–70.
Vaniman, D. T., Bish, D. L., Chipera, S. J., Flalips, C. I., Carey, J. W., Feldman, W. C. (2004). *Nature*, **431**, 663-665.
Vekilov, P. G. (2010). *Nanoscale*, **2**, 2346–2357.
Verspagen, J., Visser, P., Huisman, J. (2006). *Aquat. Microb. Ecol.* **44**, 165–174.
Vilella, K., Choblet, G., Tsao, W. -E., Deschamps, F. (2020). *J. Geophys. Res. Planets* **125**, e2019JE006248.
Vu, T. H., Hodyss, R., Choukroun, M., Johnson, P. V. (2016). *Astrophys. J. Lett.* **816**, L26.
Vu, T, H., Choukroun, M., Hodyss, R., Johnson, P. V. (2020). *Icarus*, **349**, 113746.
Vincent, W. F., Mueller, D., Van Hove, P., Howard-Williams, C. (2004). In *Origins* (pp. 483–501). Springer, Dordrecht.
Walker, C. C., Schmidt, B. E. (2015). *Geophys. Res. Lett.* **42**, 712–719.
Walsh, A., Ball, T., Schultz, D. M. (2019). *Scientific Reports*, **9**, 2349(7pp).
Wang, A., Freeman, J. F., Jolliff, B. L., Chou, I.-M. (2006). *Geochim. Cosmochim. Acta*, **70**, 6118–6135.
Wang, Y.-W., Kim, Y.-Y., Christenson, H. K., Meldrum, F. C. (2012). *Chem. Commun.* **48**, 504–506.
Wasson, J. T., Kallemeyn, G. W. (1988). *Phil. Trans. R. Soc. Lond. A*, **325**, 535–544.
Waite Jr, J. H., Combi, M. R., Ip, W.-H., Cravens, T. E., McNutt Jr., R. L., Kasprzak, W., Yelle, R. Luhmann, J., Miemann, H., Gell, D., Magee,, B., Fletcher, G., Lunine, J., Tseng, W.-L. (2006). *Science*, **311**, 1419–1422.
Waite, J. H., Glein, C. R., Perryman, R. S., Teolis, B. D., Magee, B. A., Miller, G., Grimes, J., Perry, M. E., Miller, K. E., Bouquet, A., Lunine, J. I., Brockwell, T., Bolton, S. J. (2017). *Science*, **356**, 155–159.
Williams, A. P., Longfellow, C. E., Freier, S. M., Kierzek, R., Turner, D. (1989). *Biochem.* **28**, 4283–4291.
Wollenburg, J. E., Katlein, C., Nehrke, G. and 12 others. (2018). *Nature Scientific Reports*, **8**, 1–9.
Wollenburg, J. E., Iversen, M., Katlein, C., Krumpen, T., Nicolaus, M., Castellani, Peeken, I., Flores, H. (2020). *The Cryosphere*, **14**, 1–14.
Yakovlev, S. Downing, K. H. (2011). *J. Microsc.*, **244**, 235–247.
Yancey, P. H., Gerringer, M. E., Drazen, J. C., Rowden, A. A., Jamieson, A. (2014). *Proc. Nat. Acad. Sci.* **111**, 4461–4465.
Yue, W., Yang, J. (2020). *Ap. J. Lett.* **898**, L19(8pp).
Zimmer C., Khurana, K. K., Kivelson, M. G. (2000). *Icarus* **147**, 329–347.
Zolotov, M. Y. (2012). *Icarus*, **220**, 713–729.
Zolotov, M. Y., Kargel, J. S. (2009). in *Europa* ed. R. Pappalardo, W. B. McKinnon, and K. Khurana (Tucson, AZ: Univ. Arizona Press), p431.
Zolotov, M. Y., Shock, E. L., (2001). *J. Geophys. res.* **106**, 32815–32827.